Title: Perforin-mediated pore formation at the lytic synapse triggers the canonical pyroptotic cell death pathway

Authors: Brienne McKenzie[1#], Marie-Pierre Puissegur[1#], Lucie Demeersseman[1], Frecia Rodriguez[1], Emma Cini[1], Ashwin Jainarayanan[2], Marcus A. Widdess[2], Claire C. Staton[2], Lina Chen[2], Vincent Sibaud[3], Laurence Lamant[4], Michael Dustin[2], Agathe Bernand[1], Sabina Müller[1], Salvatore Valitutti[1,4*]

Affiliations:

[1]Institut National de la Santé et de la Recherche Médicale (INSERM) UMR1037, Centre de Recherche en Cancérologie de Toulouse (CRCT), Toulouse, France. Centre National de la Recherche Scientifique (CNRS) UMR5071, Toulouse, France. Université de Toulouse III-Paul Sabatier, 31037 Toulouse, France.
[2]Kennedy Institute of Rheumatology, Nuffield Department of Orthopaedics, Rheumatology and Musculoskeletal Sciences, University of Oxford, Oxford, UK
[3]Department of Oncodermatology, Institut Universitaire du Cancer-Oncopole de Toulouse, Toulouse, FR
[4] Department of Pathology, Institut Universitaire du Cancer-Oncopole de Toulouse (IUCT), Toulouse, France

Keywords: Cyotoxic T lymphocytes, pyroptosis, programmed cell death, inflammasome, caspase-1, gasdermin D, perforin, supramolecular attack particles

***Corresponding author:** Salvatore.valitutti@inserm.fr

# These authors contributed equally to this manuscript

ABSTRACT:

Prokaryotic pore-forming toxins drive inflammasome activation and pyroptosis through K^+-dependent activation of the canonical NLRP3/caspase-1/gasdermin D signaling axis. In this study, we hypothesized that perforin, a eukaryotic pore-forming protein released into the lytic synapse by antigen-specific cytotoxic T lymphocytes (**CTLs**) upon cognate antigen recognition, mimics the pro-pyroptotic activity of ancestral pore-forming toxins, complementing its role as a conduit for granzymes. Utilizing imaging and molecular approaches, we demonstrate that perforation of target cells upon CTL attack elicits swift K^+ efflux followed by NLRP3-dependent activation of proinflammatory caspase-1 and its major substrate, the pyroptotic executioner gasdermin D (**GSDMD**). Acute target cell death upon CTL attack is gasdermin-dependent and demonstrates morphological and molecular features of pyroptosis, including pyroptotic body formation, cell bloating, plasma membrane rupture, and release of intracellular contents. Perforation of target cells by soluble perforin is sufficient to trigger rapid K^+ efflux, caspase-1 activation, and pyroptosis. By contrast, sustained interaction with CTLs unmasks a delayed apoptotic phenotype in the remaining target cells. Interestingly, exposure of target cells to exogenous supramolecular attack particles (**SMAPs**) recapitulates this apoptotic phenotype, suggesting that soluble perforin and SMAPs play dichotomous roles in target cell death. Our results reveal a novel mechanism for engagement of pyroptotic machinery upon CTL attack, in which perforin itself can autonomously engage programmed cell death (**PCD**), highlighting the complexity and diversity of the CTL lytic arsenal.

INTRODUCTION

$CD8^+$ cytotoxic T lymphocytes (**CTLs**) are potent, sensitive effector cells of the adaptive immune system, which eliminate target cells upon recognition of cognate antigen using a variety of cytotoxic strategies, including exocytosis of soluble cytotoxic molecules, death receptor ligation, and release of particulate killing entities known as supra-molecular attack particles (**SMAPs**)[1-3].

SMAPs are characterized by a glycoprotein shell within which are encapsulated a variety of different molecules, including cytotoxic granzymes and a variety of chemokines[4]. Isolated SMAPs have been shown to kill target cells over a timeframe of hours to days[4,5], but their precise mechanism of killing remains elusive.

By contrast, the perforin/granzyme pathway is well-characterized, ultra-rapid pathway that involves directional secretion of soluble cytotoxic molecules within specialized regions at the CTL-target cell interface termed lytic synapses (**LS**). Within seconds of lytic granule release, perforation of the target cell membrane by the pore-forming protein perforin occurs; this facilitates delivery of soluble monomeric granzymes, cytotoxic proteases that cleave intracellular substrates and engage the target cell's caspase network to promote programmed cell death (**PCD**)[6]. When the target cell's plasma membrane is perforated, Ca^{2+} influx into the target cell can activate ultra-rapid Ca^{2+}-dependent reparative mechanisms at the LS (including lysosomal exposure and ESCRT-mediated membrane repair)[7-10] that dampen CTL-mediated cytotoxicity by promoting membrane repair and perforin degradation. Whether an individual target cell ultimately succumbs to CTL attack depends upon the accumulation of intracellular damage events inflicted by attacking CTLs, weighed against the ultimately finite reparative resources of the target[11,12]. Thus, the LS provides the spatiotemporal context within which different pro-survival and pro-death processes interact and compete to determine target cell fate.

67 Within this context, perforin plays a particularly crucial role in ultra-rapid lethal hit delivery,
68 undergoing a transformation (at neutral pH and in the presence of Ca^{2+}) from soluble secreted
69 monomers to complex oligomeric transmembrane pores that breach the target cell plasma
70 membrane and provide the physical conduit for trafficking of soluble cytotoxic granzymes into the
71 cytosol[6,13-15]. However, this well-studied function may overshadow additional biologically
72 significant functions that emerge independently of granzyme entry as a result of perforin's pore-
73 forming properties. Perforin is a member of the diverse and ancient class of pore-forming proteins
74 (**PFPs**), and more specifically the membrane attack complex perforin/cholesterol-dependent
75 cytolysin (**MACPF/CDC**) super-family, which includes eukaryotic proteins such as the membrane
76 attack complex (**MAC**) of the complement cascade, as well as prokaryotic pore-forming virulence
77 factors such as streptolycin O (**SLO**) and listeriolysin O (**LLO**)[14,16,17]. Perforation of the eukaryotic
78 plasma membrane by PFPs has an array of intracellular consequences, including the perturbation
79 of local osmotic and electrochemical gradients (particularly K^+ and Ca^{2+} homeostasis) as a result
80 of compromised plasma membrane integrity and directional ion flux through transmembrane
81 pores[18]. This ion flux activates a multitude of downstream signaling cascades, including cell stress
82 responses, membrane repair, inflammation, and in some cases, PCD[18,19].

83 One particularly important consequence of plasma membrane perforation by PFPs is the activation
84 of one or more K^+-sensitive inflammasomes (e.g. NLRP3[20-22]), multi-protein complexes that
85 mediate the proximity-induced auto-proteolysis of inflammatory caspases such as caspase-1[22-27].
86 In addition to mediating cytokine secretion in certain cells, canonical inflammasome activation can
87 also trigger the activation of gasdermin D (**GSDMD**), a member of the gasdermin family of pore-
88 forming executioner proteins responsible for driving **pyroptosis** ("fiery death"), a lytic and
89 proinflammatory PCD modality[28-31]. Upon activation, cleaved GSDMD translocates to the plasma

membrane, where it oligomerizes and forms stable pores[32,33], which are impermeable to large molecules such as lactate dehydrogenase (**LDH**)[34] but selectively permeable to positively charged ions and small non-acidic proteins (e.g. mature interleukin (**IL**)-1β)[35-38]. In cells with highly functional membrane repair mechanisms, GSDMD pores can be removed, rendering pyroptosis reversible at very early stages[39-42]. Otherwise, loss of membrane integrity leads to a collapse in electrochemical gradients, driving a rapid influx of water through GSDMD pores[34,43]. This causes a characteristic "necrotic" cell death morphology[44], characterized by cell bloating/swelling and formation of pyroptotic bodies, bubbling membrane protrusions that swell and contract stochastically in response to changing osmotic conditions[37,45,46]. Late-stage pyroptosis often involves catastrophic plasma membrane rupture (**PMR**), which releases proinflammatory alarmins (e.g. high mobility group box 1, **HMGB1**) and large cytoplasmic molecules (e.g. LDH) into the microenvironment. Although multiple pyroptotic pathways have since been identified (reviewed in [28,37,47]), this "canonical" NLRP3/caspase-1/GSDMD pathway remains a widely recognized and crucial pillar of innate immunity.

Within the context of CTL attack, apoptosis has been classically considered the main mediator of CTL-mediated target cell death, yet evidence for inflammatory, immunogenic and non-apoptotic cell death modalities upon CTL attack has also been gradually accumulating in the literature[48-52]. Most recently, several studies have provided direct evidence to support granzyme-mediated pyroptosis upon T cell attack[53-55]. These findings have prompted the re-examination of CTL-mediated killing through the lens of a more nuanced contemporary understanding of non-apoptotic PCD modalities[56], and highlighted how different cytotoxic molecules may each have their own unique manner of engaging the target cell's PCD pathways.

112 In this study, we hypothesize that pore formation by perforin can activate the same inflammatory
113 pro-pyroptotic pathways associated with ancestral pore-forming toxins, independently of cytotoxic
114 granzymes. We utilized imaging and molecular approaches to test the hypothesis that perforin-
115 mediated pore formation upon attack by human antigen-specific CTLs activates the canonical
116 pyroptotic signaling pathway in transformed target cells. We provide evidence that the pyroptosis-
117 initiating signal originates at the LS, whereupon perforin-mediated pore formation leads to rapid
118 K^+ efflux and activation of the canonical NLRP3/caspase-1/GSDMD pathway. Conversely, we
119 show that sustained interaction with CTLs unmasks a delayed apoptotic phenotype in the remaining
120 target cells. Exposure of target cells to exogenous SMAPs preferentially triggered apoptosis
121 indicating that perforin and SMAPs activate parallel death pathways, with perforin triggering
122 pyroptosis and SMAPs steering the target towards apoptosis. Collectively these results provide
123 evidence for a proinflammatory perforin-dependent caspase-1/GSDMD pyroptotic signaling
124 cascade upon target perforation that contrasts with SMAP-induced apoptotic cell death revealing
125 novel mechanisms for engagement of pyroptotic/apoptotic machinery upon CTL attack, and
126 highlighting the complexity, diversity, and versatility of the CTL lytic arsenal.

127

128

129

130 **RESULTS**

131 *Potassium efflux is observed in target cells upon perforation by CTLs*

132 To investigate whether a canonical pyroptotic signaling cascade is induced downstream of target
133 cell perforation, we first utilized a multi-cell system wherein clonal antigen-specific human CTLs
134 were conjugated with JY cells (an Epstein Barr virus (**EBV**)-transformed human B cell line used
135 as a conventional target for human CTLs[57]), which had been pulsed or not with 10μM cognate
136 antigenic peptide (peptide from human cytomegalovirus protein pp65); this well-characterized
137 system enabled us to focus upon the target cell response to CTL attack, in the context of strong
138 antigenic stimulation and optimal CTL activation as previously described[7,8,58,59]. JY cells are
139 known to be highly sensitive to CTL attack[7,8,58], providing a suitable model system for investigating
140 CTL-induced target cell death.

141 Since the insertion of pore-forming toxins (such as aerolysin[23], *C. perfringens* β-toxin[60], *S. aureus*-
142 derived PVL[26], *T. pyogenes*-derived pyolysin[27]) into the plasma membrane are known to drive
143 rapid K^+ efflux (reviewed in [18]), we hypothesized that perforin pore formation may likewise trigger
144 disruption of intracellular K^+ homeostasis in target cells upon CTL attack, thus providing an
145 activating signal to NLRP3, the prototypic K^+-sensitive canonical inflammasome[20-22]. Although
146 perforin pores are known to be selectively permeable to cationic cargo[15], direct assessment of K^+
147 loss upon target perforation by human CTLs is largely absent from the literature. To address this
148 question, we made use of the well-described cell membrane-permeable fluorescent K^+ indicator,
149 Ion Potassium Green-2 AM (IPG-2 AM; formerly Asante Potassium Green-AM, APG-AM[61]),
150 which has been widely used to assess intracellular K^+ concentration (**$[K^+]_i$**) using both imaging and
151 flow cytometry approaches[62-64]. Prior to assessing K^+ in target cells upon CTL attack, we first
152 validated our flow cytometry approach using nigericin, a well-characterized bacterially-derived K^+

153 ionophore whose primary mechanism of action is the reduction of $[K^+]_i$ through K^+/H^+ exchange[65-
154 67], and which has been previously validated using APG-AM probes[63]. As shown in
155 **Supplementary Figure 1a-c**, IPG-2 AM intracellular fluorescent signal decreased in a time-
156 dependent manner upon exposure of JY cells to nigericin, confirming that a reduction in $[K^+]_i$ is
157 indeed detectable in JY cells using this flow cytometry approach.

158 To assess changes in intracellular K^+ upon CTL attack, non-pulsed and cognate antigen-pulsed
159 target cells were loaded with IPG-2 AM, conjugated with CTLs for 5 or 15min at various
160 effector:target (**E:T**) ratios, and subjected to analysis by flow cytometry in the presence of a
161 viability dye. As shown in **Figure 1a-d** , a rapid and E:T ratio-dependent loss of intracellular K^+
162 was observed in antigen-pulsed target cells upon 5 and 15min conjugation with CTLs; the majority
163 of K^+ efflux occurred rapidly upon CTL attack (ie within the first 5min of conjugation, **Figure**
164 **1a,c**). Dead cells were excluded from this analysis, supporting the interpretation that the IPG-2
165 AM^{dim} population identified in **Figure 1a-d** contained viable cells with diminished $[K^+]_i$ rather
166 than simply dead cells.

167

168 *Soluble human perforin is sufficient to initiate potassium efflux*

169 We next sought to assess whether soluble perforin alone was sufficient to initiate K^+ efflux from
170 perforated target cells in the absence of cytotoxic granzymes. A rapid and dose-dependent loss of
171 intracellular K^+ was indeed observed in JY cells upon exposure to soluble perforin, at 5 and 15min,
172 based on the reduction of the percentage of IPG-2 AM^{bright} cells (**Figure 1e-g**). To illustrate that
173 this reduced signal was specific to loss of K^+ and not merely leakage of IPG-2 AM out of perforated
174 cells, a parallel set of experiments was conducted in which soluble perforin was applied to JY cells

175 in the presence of excess extracellular K^+, conditions under which the flow of K^+ ions out of the
176 perforated cell is inhibited[20,22,68]. As shown in **Supplementary Figure 2a**, performing the
177 experiments in high [K^+] buffer rescued perforin-induced IPG-2 AM signal reduction, supporting
178 the interpretation that loss of IPG-2 AM signal in perforin-exposed cells was indeed attributable
179 specifically to K^+ efflux.

180

181 *Caspase-1 activity is detectable in target cells upon CTL attack*

182 We next sought to test the hypothesis that caspase-1, the canonical inflammatory caspase, was
183 activated in target cells upon CTL attack downstream of K^+ efflux. To accomplish this, we first
184 verified full-length caspase-1 expression at baseline in JY cells, using the triple-negative breast
185 cancer line MDA-MB231 as a positive control[69,70] (**Supplementary Figure 3a**). To test whether
186 caspase-1 became activated specifically in targets upon CTL attack, we utilized a well-validated
187 cell-permeable activity-dependent fluorescent probe that irreversibly binds to active caspase-1
188 through covalent coupling[71,72]. This highly sensitive approach enabled the quantification of
189 caspase-1 activity at the single-cell level by flow cytometry. To first validate this system, JY cells
190 were exposed to nigericin (described above), a well-characterized and widely utilized activator
191 caspase-1[73,74], and caspase-1 assessed by flow cytometry. Compared to solvent-treated controls,
192 nigericin exposure resulted in a significant increase in the percentage of cells displaying caspase-1
193 activity (**Supplementary Figure 3b**). To assess caspase-1 activity in target cells upon CTL attack,
194 CTLs were conjugated with antigen-pulsed or non-pulsed JY cells that had been pre-loaded with
195 the caspase-1 probe; after 5 and 15min conjugations, the conjugates were disrupted and subjected
196 to flow cytometry (gating strategy shown in **Supplementary Figure 3c**). Under these conditions,
197 both the percentage of target cells with high caspase-1 activity (**Figure 2a,b**) and the median

198 caspase-1 fluorescence intensity **(Figure 2a,c)** significantly increased following CTL conjugation,
199 compared to non-pulsed controls. To validate the specificity of this read-out, we transfected JY
200 cells with either non-targeting or *CASP1*-targeting siRNA (siRNA validation shown in
201 **Supplementary Figure 3d**) and demonstrated that caspase-1 activity in antigen-pulsed cells
202 (normalized to non-pulsed controls) was significantly decreased in the *CASP1* siRNA-transfected
203 condition compared to non-targeting siRNA-transfected controls (**Supplementary Figure 3e**).

204 We next tested whether caspase-1 activity upon CTL attack was antigen-dose dependent. Target
205 cells were pulsed with different concentrations of peptide (from 1nM to 10μm) and conjugated
206 with CTLs for 15 min; a significant increase in the percentage of cells with high caspase-1 activity
207 was observed with as little as 1nM antigenic peptide (**Figure 2d**). We performed a similar analysis
208 to assess the effect of E:T ratio, wherein cells were pulsed with 10μm of antigen and subsequently
209 conjugated with CTLs at an E:T ratio of 0.25, 1, or 4. As shown in **Figure 2e**, the percentage of
210 cells with high caspase-1 activity increased proportionally to E:T ratio, with an E:T ratio as low as
211 0.25 resulting in a detectable increase in caspase-1 activity after 15min conjugation.

212

213 *Caspase-1 activity is diminished upon NLRP3 knockdown*

214 Although various potassium-sensitive inflammasomes can serve as a platform for caspase-1
215 activity, the NLRP3 inflammasome was of specific interest in this study since it is well-known to
216 be activated by pore-forming toxins in a potassium-dependent manner[22-27]. To test whether NLRP3
217 was involved in caspase-1 activation upon CTL attack, we first verified NLRP3 protein expression
218 in our target cells of interest (**Supplementary Figure 3a**) before assessing whether NLRP3
219 deficiency affected caspase-1 activity following CTL attack. We compared the fold increase in

220 caspase-1 fluorescence intensity in targets that had been transfected with either non-coding or
221 *NLRP3*-targeting siRNA (validation shown in **Supplementary Figure 3d**) and subsequently
222 conjugated with CTLs. This analysis revealed a consistent decrease in caspase-1 fluorescence
223 intensity when NLRP3 was knocked down compared to non-targeting controls (**Figure 2f**). The
224 modest nature of this decrease is not unexpected considering that there are alternative
225 inflammasomes that can be engaged under stress conditions to process caspase-1 (e.g. NLRP1,
226 which detects abnormal protease activity and may also be sensitive to K^+ concentration[68,75] and
227 NLRC4, which has been shown to be activated alongside NLRP3 in response to bacterial pore
228 forming toxins[24]). Nonetheless, these data suggest a role for the NLRP3 inflammasome in this
229 signaling axis upstream of caspase-1 activation.

230

231 *Caspase-1 and caspase-3 activity are often detectable in the same cells upon CTL attack*

232 Caspase-3 is a well-characterized dual-function caspase that can either initiate apoptosis or
233 GSDME-mediated pyroptosis; it is known to be robustly activated upon CTL attack[54,55,76,77]. As
234 such, we next assessed activation of caspase-3 under parallel conditions as caspase-1, utilizing a
235 cell-permeable activity-dependent fluorescent probe. As expected, these experiments confirmed a
236 significant time-dependent and antigen dose-dependent activation of caspase-3 following 5 and
237 15min conjugation of target cells with CTLs (**Supplementary Figure 4a,b**), which paralleled our
238 observations with caspase-1. As little as 1nM of antigenic stimulation was sufficient to induce
239 significant caspase-3 activity when pulsed cells were conjugated with CTLs (**Supplementary**
240 **Figure 4b**). We then conducted double-staining experiments to determine whether caspase-1 and
241 caspase-3 activity were detectable in the same cells (**Supplementary Figure 4c**). These
242 experiments revealed a significant caspase-1 single-positive population, along with a double-

243 positive population at both time points tested; caspase-3 single-positive cells remained relatively
244 rare. Collectively, these data suggest that the two caspases are indeed frequently (but not
245 exclusively) activated in the same cells upon CTL attack, and that caspase-1 can be activated prior
246 to (or in the absence of) caspase-3.

247

248 *Caspase-1 activity is perforin-dependent and soluble perforin activates caspase-1*

249 We next sought to determine whether caspase-1 activation upon CTL attack required the perforin
250 secretory pathway by pre-treating CTLs with the well-established carboxylic ionophore monensin
251 to increase lytic granule pH, as described previously[7,8,78]. Interfering with the pH of lytic granules
252 has been shown to markedly attenuate perforin-mediated cytotoxicity[7,79]. Herein, we pre-treated
253 CTLs with monensin prior to conjugation with pulsed or non-pulsed targets; as shown in **Figure**
254 **2g**, monensin pre-treatment of CTLs largely abrogated target cell caspase-1 activity, supporting the
255 interpretation that the perforin secretory pathway is needed for caspase-1 activation.

256 We then tested whether target perforation by soluble perforin was sufficient to activate the caspase-
257 1 pathway. As shown in **Figure 2h**, treatment with soluble perforin for 15min significantly
258 increased the percentage of cells with high caspase-1 activity. To assess whether this caspase-1
259 activity was dependent upon upstream K^+ efflux as a result of target perforation, we performed the
260 same experiments in the presence of excess extracellular K^+ to limit K^+ efflux from perforated
261 targets (as above). When the assays were performed in high [K^+] perforin binding buffer, caspase-
262 1 fluorescence intensity in perforin-exposed cells was reduced compared to cells in the standard
263 perforin-binding buffer (**Figure 2i**). This supported the hypothesis that caspase-1 activity in
264 perforated target cells was dependent upon K^+ efflux.

265 Collectively, these data support a model wherein perforin-mediated pore formation leads to swift
266 K^+ efflux from perforated cells, leading to activation of the potassium-sensitive NLRP3
267 inflammasome and the caspase-1 pathway.

268

269 *Target cells express multiple gasdermins at the transcript and protein level*

270 Knowing that caspase-1 was activated in target cells upon CTL attack, we next sought to determine
271 whether GSDMD, a canonical executioner of pyroptosis and the quintessential substrate of
272 caspase-1, was likewise activated following CTL attack. GSDMD has been proposed to have a
273 role in anti-tumor immunity[80] but its activation in the context of CTL attack has never been
274 demonstrated. It is known that gasdermins are expressed to varying degrees in transformed and
275 untransformed cells[28,38], and to test this we first assessed transcript expression of *GSDMA-E* at
276 baseline in JY cells and a diverse panel of other target cells. As shown in **Supplementary Figure**
277 **5a**, *GSDMD* and *GSDME* were the most highly and consistently expressed of the five gasdermins
278 at baseline across a range of target cells. We validated GSDMD expression at the protein level in
279 two well-characterized target cell lines: JY (described above) and D10, a well-characterized
280 melanoma cell line, moderately resistant to CTL attack due to reparative membrane turnover[7,8,81].
281 MDA-MB231 (previously shown to highly express GSDMD[82] and GSDME[83]) was used as a
282 positive control. Consistent with transcript data, full-length GSDMD protein was detectable in all
283 three cell lines at baseline (**Supplementary Figure 5b**). Specificity of the GSDMD antibody was
284 validated using siRNA approaches, wherein GSDMD signal was strongly reduced in *GSDMD*-
285 targeting siRNA-transfected but not *GSDME*-targeting siRNA-transfected JY cells
286 (**Supplementary Figure 5c**).

287

288 *Cleaved GSDMD accumulates in target cells upon attack by CTLs and is enriched near the*
289 *immunological synapse*

290 To assess the accumulation of cleaved GSDMD in target cells upon conjugation with CTLs, we
291 profited from two commercially available and widely utilized antibodies[84-87]: the first specifically
292 detects the active N-terminal of GSDMD ("cleaved GSDMD") but not full-length GSDMD; and
293 the second (also utilized for immunoblots above) detects both full-length and cleaved GSDMD
294 ("total GSDMD"). JY cells were conjugated with CTLs for 15min, fixed, permeabilized, and
295 stained with antibodies against cleaved GSDMD, total GSDMD, and perforin before being
296 subjected to confocal microscopy. As shown in the illustrative 3D reconstruction in **Figure 3a**,
297 total but not cleaved GSDMD immunoreactivity is detectable in non-pulsed target cells interacting
298 with CTLs; however, upon interaction of pulsed JY cells with CTLs and initiation of target cell
299 death, target cells display a high degree of cleaved GSDMD immunoreactivity, frequently
300 associated with the bubbling morphology typical of pyroptosis. To facilitate quantification of
301 cleaved GSDMD immunoreactivity in target cells upon CTL attack, we next focused upon CTL-
302 target cell conjugates where lytic granules were polarized towards the target but the target was not
303 yet excessively bubbling. As shown in **Figure 3b-e**, while total GSDMD immunoreactivity was
304 equivalent in both non-pulsed and pulsed target cells interacting with CTLs (**Figure 3d**), cleaved
305 GSDMD MFI was significantly increased in targets under pulsed conditions after 15min
306 conjugation (**Figure 3e**). JY cells transfected with siRNA targeting *GSDMD* exhibited significantly
307 reduced fluorescent signal from the cleaved GSDMD antibody upon interaction with CTLs
308 compared to non-targeting siRNA-transfected controls (**Supplementary Figure 6a-c**).

309 Upon visual examination of cleaved GSDMD immunoreactivity in pulsed target cells upon CTL
310 attack (**Figure 3b**), it became apparent that while total GSDMD was evenly distributed throughout
311 the target cell, cleaved GSDMD immunoreactivity appeared concentrated near the LS in a subset

312 of pulsed target cells, suggesting that the initial signal to activate GSDMD may first be triggered
313 locally near the LS. To quantify this observation, we assessed both cleaved and total GSDMD MFI
314 in the synaptic half versus the distal half of pulsed target cells in conjugates with CTLs and
315 generated a ratio of synaptic MFI /distal MFI; in this analysis, a ratio >1 indicated synaptic
316 enrichment of the protein of interest, a ratio = 1 indicated even distribution throughout the cell, and
317 a ratio <1 indicated distal enrichment of the protein of interest. As shown in **Supplementary**
318 **Figure 7**, after 15min conjugation, total GSDMD was evenly distributed throughout target cells in
319 conjugation with CTLs under non-pulsed and pulsed conditions. However, cleaved GSDMD
320 (which was only consistently detectable under antigen-pulsed conditions) was frequently enriched
321 on the synaptic side of the target cell. To determine whether this phenomenon might occur even
322 more dramatically at earlier timepoints, we performed the same analysis after only 5min
323 conjugation. As shown in **Figure 3f-i,** cleaved GSDMD (but not total GSDMD) was significantly
324 enriched in target cells upon CTL attack even at this early time point. Likewise, cleaved GSDMD
325 was strongly enriched near the LS, while total GSDMD was evenly distributed throughout the cell
326 (**Figure 3j,k**). This observation was conceptually consistent with a localized synaptic trigger for
327 GSDMD activation.

328 *Target cell death upon attack by human Ag-specific CTL is characterized by membrane bubbling*
329 *and loss of membrane integrity typical of pyroptosis*

330 Having established that the K^+/NLRP3/caspase-1/GSDMD canonical pyroptotic pathway was
331 activated in target cells upon CTL attack, we next sought to determine whether target cell death
332 displayed the quintessential molecular and morphological indicators of pyroptosis. To address this,
333 we first utilized time-lapse microscopy to visualize target cell death. Although microscopy alone
334 does not distinguish amongst the various types of programmed necrosis (pyroptosis, necroptosis,
335 etc.), time-lapse microscopy remains a powerful and pragmatic approach for identifying the

336 quintessential morphological features of non-apoptotic PCD modalities (such as swelling,
337 membrane bubbling, plasma membrane rupture, and vital dye uptake)[44]. To visualize cell death
338 morphology, target cells were pulsed (or not) with cognate antigen for 2hr and conjugated with
339 antigen-specific CTLs in the presence of low-concentration (6.6 µg/mL) PI, which served as a vital
340 dye. As expected, non-pulsed target cells displayed transient non-lethal interactions with CTLs
341 (**Supplementary Figure 8a,d)**, while antigen-pulsed JY cells readily formed conjugates with
342 CTLs, and of these, 78% became PI^+ within 120min (**Supplementary Figure 8b,c**).

343 Using this system, we sought to observe and quantify the morphological features of target cell
344 death upon CTL attack. In the example shown in **Figure 4a** and **Supplementary Movie 1**, CTL
345 target recognition was indicated by Ca^{2+} flux and polarization of the CTL's microtubule organizing
346 centre (**MTOC**) towards the LS. Rapidly thereafter, the target displayed irregular bubbling
347 membrane protrusions, which expanded and contracted in the stochastic, erratic manner typical of
348 pyroptotic bodies[37,46]. This bubbling was followed by cessation of cellular motility, bloating of the
349 target, and ultimately explosive PMR, concurrent with instantaneous PI influx, all of which are
350 prototypical morphological signs of pyroptosis and other necrotic cell death modalities[44]. These
351 observations were recapitulated in the second example shown in **Figure 4b** and **Supplementary**
352 **Movie 2** (wherein PI influx was slightly more gradual), as well as additional examples from three
353 independent experiments (**Supplementary Figure 8c**). Such morphological features closely
354 recapitulated the bubbling, lytic phenotype of pyroptosis exemplified by cells exposed to
355 nigericin[65,66,88], shown in **Supplementary Figure 9a,d** and **Supplementary Movies 3-5**, but
356 contrasted starkly with the morphology of apoptosis (exemplified by cells treated with the broad-
357 spectrum kinase inhibitor staurosporine[44]). As shown in **Supplementary Figure 9b,d** and
358 **Supplementary Movies 6-9**, staurosporine-treated apoptotic cell death was slow and controlled,

359 with the gradual appearance of small fragmented apoptotic bodies rather than violent swelling,
360 bubbling, or catastrophic PMR.

361 To assess cell death morphology in individual cells longitudinally, we utilized a semi-automated
362 image-processing pipeline to analyze changes in target cell size and shape over time following CTL
363 attack. Non-pulsed cells were analyzed as a control (**Supplementary Figure 10** and
364 **Supplementary Movie 10**) and revealed the mild rhythmic oscillations in size (cross-sectional
365 area) and shape (aspect ratio) typical of a live target cell. By contrast, upon CTL attack, dying
366 target cells exhibited sharp, erratic fluctuations in cross-sectional area and aspect ratio concurrent
367 with initiation of membrane bubbling, both of which stabilized upon cessation of cell motility
368 (**Supplementary Figure 11a-d** and **Supplementary Movies 11-12**). These bubbling membrane
369 protrusions combined with cell bloating caused transient expansion of target cells, with
370 representative cells exceeding 160% of their original cross-sectional area (**Supplementary Figure**
371 **11b**). This phenotype closely resembled nigericin-induced pyroptosis, wherein cross-sectional area
372 and aspect ratio varied dramatically within the bubbling phase before stabilization upon cessation
373 of cell movement (**Supplementary Figure 12a-d** and **Supplementary Movies 4-5**), with
374 representative cells swelling up to 200% of their initial cross-sectional area immediately before
375 lysis (**Supplementary Figure 12d**). By contrast, apoptotic cells' cross-sectional area and aspect
376 ratio remained relatively consistent throughout the imaging period (**Supplementary Figure 13a-**
377 **d** and **Supplementary Movies 8-9**). Collectively, these results indicated that dying target cells
378 exhibited a morphology that was consistent with pyroptosis following CTL attack.

379

380

381

382 *Target cell death upon attack by human Ag-specific CTL is lytic and inflammatory*

383 To determine whether CTL-mediated cell death also exhibited a molecular profile consistent with
384 non-apoptotic cell death modalities, antigen-specific CTLs were conjugated with antigen-pulsed or
385 non-pulsed target cells, subjected to Annexin V/PI staining and assessed by flow cytometry (gating
386 strategy in **Supplementary Figure 14**). The Annexin V/PI assay is a highly sensitive and well-
387 validated assay designed to distinguish both between early and late apoptosis, and between
388 apoptosis and programmed necrosis[44]. It is based upon the premise that FITC-conjugated Annexin
389 V binds to externalized phosphatidylserine (**PS**) on the outer membrane of apoptotic cells, prior to
390 the loss of membrane integrity and uptake of vital dyes; thus, when combined with PI as a vital
391 dye, the Annexin V/PI assay permits discrimination between live cells (double negative), early-
392 stage apoptotic cells (Annexin V single-positive), and end-stage apoptotic or necrotic cells
393 (Annexin V/PI double-positive)[44]. Necrotic cell death modalities (including pyroptosis) do not
394 accumulate a sizeable Annexin V single-positive population, and instead Annexin V staining
395 occurs concurrently with PI uptake[44]. Of note, under prolonged *in vitro* conditions wherein
396 phagocytic clearance of apoptotic cells cannot occur, end-stage apoptotic cells tend to undergo a
397 process of secondary necrosis (example shown in **Supplemental Figure 9d**), leading to the uptake
398 of vital dyes and the eventual accumulation of an AnnexinV/PI double-positive population[44]. As
399 such, the double-positive population is not a distinguishing feature between programmed necrosis
400 and late apoptosis; the important distinguishing feature in apoptosis is the presence of an Annexin
401 V single-positive population, which is absent during pyroptosis and other forms of necrotic PCD.

402 As shown in **Figure 4c-d**, Annexin V/PI double-positive target cells accumulated in a time-
403 dependent fashion after 1hr and 4hr conjugation with CTLs. Conversely, the Annexin V single-
404 positive population remained unchanged across all time points tested, consistent with a non-

405 apoptotic cell death mechanism. This closely recapitulated the phenotype of nigericin-exposed
406 pyroptotic cells, which likewise acquired a substantial double-positive population and failed to
407 accumulate an Annexin V single-positive population (**Supplementary Figure 15a,b**). By contrast,
408 a significant increase in the Annexin V single-positive population was observed following
409 staurosporine exposure (**Supplementary Figure 15a,b**), a classical feature of apoptosis that is
410 notably absent during acute CTL-mediated killing. Of note, the population of staurosporine-treated
411 cells also contained a sizeable number of Annexin V/PI double-positive (secondary necrotic) cells,
412 which is quite typical of end-stage apoptosis *in vitro*[44].

413 To assess whether CTL-mediated cell death was associated with release of lytic or inflammatory
414 molecules, supernatants were collected following conjugation of non-pulsed or antigen-pulsed
415 target cells with CTLs for 1 or 4hr. As illustrated in **Figure 4e**, the classical alarmin and
416 immunogenic cell death (**ICD**) marker HMGB1 was readily detectable in supernatant after 1hr.
417 Likewise, supernatant LDH activity was detectable after 4hr conjugation (**Figure 4f**), consistent
418 with a lytic cell death modality such as pyroptosis.

419 Collectively, these experiments indicated that target cell death upon CTL attack possessed the
420 defining morphological features and molecular profile typical of pyroptosis, including rapid
421 expansion and contraction of pyroptotic bodies, stochastic changes in cell size and shape, loss of
422 membrane integrity concurrent with PS exposure, and overt membrane lysis indicated by
423 supernatant HMGB1 and LDH activity.

424

425

426

427 *GSDMD and GSDME knockdown and knockout reduces CTL-mediated cytotoxicity*

428 As a final demonstration that CTL-mediated cell death was indeed pyroptotic, we asked whether
429 inhibition of pyroptotic pathways would have a measurable effect on target cell death upon CTL
430 attack. As described above, JY cells express high levels of two pyroptotic executioners (GSDMD
431 and GSDME) at the transcript and protein levels, which enables them to undergo pyroptosis either
432 through the caspase-1/GSDMD pathway described above or the caspase-3/GSDME pathway
433 identified by others[54,55]. To inhibit both pathways simultaneously, we transfected JY cells with
434 either non-targeting siRNA or a combination of both *GSDMD*- and *GSDME*-targeting siRNAs;
435 knockdowns were validated by immunoblot (**Supplementary Figure 16a**). Transfected target cells
436 were pulsed or not with antigenic peptide and conjugated with CTLs for 4hr before being subjected
437 to Annexin V/PI analysis, while supernatants were collected for LDH assay. As shown in
438 **Supplementary Figure 16b**, concurrent knockdown of both pyroptotic pathways significantly
439 inhibited the accumulation of Annexin V/PI double-positive cells (**Supplementary Figure 16b**),
440 compared to the non-targeting siRNA condition; no increase in Annexin V single-positive cells
441 was observed within this time frame, indicating that the inhibition of *GSDMD* and *GSDME* did not
442 lead to a compensatory increase in apoptosis at these time points. However, knockdown of the
443 pyroptotic pathways did prevent the loss of the double-negative population, which indicated that
444 cells remained in a healthy state and failed to undergo either pyroptotic or apoptotic cell death in
445 the time frame examined. No difference in the PI single-positive population was observed. To
446 validate these observations in a knock-out system, these experiments were repeated using *GSDMD*
447 and *GSDME* double knock-out target cells generated using the Crispr Cas9 system (validation
448 shown in **Supplementary Figure 16c**). These results recapitulated our observations from the
449 siRNA experiments, whereupon loss of both pyroptotic executioners significantly inhibited the

450 accumulation of Annexin V/PI double-positive cells upon CTL attack (**Supplementary Figure**
451 **16d**). Collectively, these results illustrate that CTL-mediated end-stage cell death is dependent
452 upon the pyroptotic executioners GSDMD and GSDME.

453 To further examine the effect of *GSDMD* and *GSDME* loss on the cell death phenotype, LDH
454 activity was assessed in both non-targeting siRNA-transfected and *GSDMD*/*GSDME* double
455 knockdown JY cells upon CTL attack. As anticipated, knockdown of both pyroptotic executioners
456 led to a significant decrease in supernatant LDH activity (**Supplementary Figure 16e**) in pulsed
457 conditions. Interestingly, caspase-1 and caspase-3 were equivalently activated in target cells
458 bearing the *GSDMD/GSDME* double knockdown compared to non-targeting siRNA-transfected
459 controls (**Supplementary Figure 16f,g**). This offered the crucial piece of insight that even when
460 executioner caspases are fully activated in target cells upon CTL attack, those target cells do not
461 die as efficiently without the pyroptotic executioners GSDMD and GSDME as caspase substrates.

462

463 *Target cell pyroptosis is dependent upon the perforin pathway and soluble perforin activates*
464 *pyroptosis*

465 To next determine if target cell pyroptosis was dependent upon the perforin pathway, we utilized
466 monensin (described above) to attenuate the toxicity of the perforin/granzyme pathway through
467 acidification of CTL lytic granules. As shown in **Figure 4g-h**, target cells conjugated with
468 monensin-treated CTLs failed to accumulate an Annexin V/PI double-positive population,
469 indicating that pyroptosis requires intact perforin signaling.

470 In a second approach, we assessed whether exposure of JY cells to soluble perforin could trigger
471 pyroptotic cell death. To assess this, we exposed JY cells to recombinant perforin for 60min and
472 assessed cell death utilizing the Annexin V/PI assay. Consistent with a pyroptotic cell death

473 modality, perforin exposure resulted in a significant increase in Annexin V/PI double-positive cells
474 (**Figure 4i**) but no increase in Annexin V single-positive cells (which would indicate apoptosis).
475 Moreover, no increase in PI single-positive cells was apparent, which argued against overt (non-
476 programmed) necrotic cell death occurring from perforin-induced osmotic shock. Unlike
477 pyroptosis, non-programmed necrotic phenomena such as osmotic shock cannot be prevented or
478 delayed through pharmacological or genetic intervention[56]; to further illustrate that perforin-
479 mediated cell death was programmed rather than overtly necrotic, we pre-treated JY cells with VX-
480 765, a well-validated, highly specific and cell-permeable peptidomimetic caspase-1 inhibitor[85,89,90].
481 Compared to solvent-treated controls, cells that were pre-treated with VX-765 showed a significant
482 reduction in perforin-induced cell death (**Figure 4j**), illustrating that soluble perforin induced
483 caspase-1-mediated PCD under these conditions.

484 With this insight, we next sought to determine whether the canonical pyroptotic pathway was
485 activated upon CTL attack in a broader panel of transformed human cells.

486 *Melanoma cells activate pyroptosis upon CTL attack*

487 To systematically test whether human melanoma cells could also undergo pyroptosis upon CTL
488 attack, we performed Annexin V/PI assays using three different cellular systems, including D10
489 and LB2259-MEL.A melanoma cells that have been previously characterized[7,8], as well as cells
490 isolated on-site from a patient melanoma sample (Toulouse Melanoma 3, or TouM3). These
491 different target cells were conjugated with CTLs for 4hr, subjected to Annexin V/PI staining, and
492 assessed by flow cytometry.

493 As shown in **Figure 5a-b**, Annexin V/PI double-positive target cells accumulated in all cell lines
494 tested upon 4hr conjugation with CTLs, whereas the Annexin V single-positive population

495 remained unchanged compared to non-pulsed controls (**Figure 5c**), consistent with a pyroptotic
496 cell death mechanism. The percentage of PI single-positive cells did not change in any cell line
497 tested (**Figure 5d**).

498 Based on these observations, we utilized the D10 melanoma cell line (which is known to be
499 moderately resistant to CTL attack due to enhanced reparative membrane turnover[7,8,58,81]) to
500 determine whether partially resistant cells activate the caspase-1 and whether inhibition of
501 defensive membrane turnover increases signaling through this pyroptotic pathway. After first
502 verifying that D10 cells expressed NLRP3, caspase-1, GSDMD, and GSDME at the protein level
503 at baseline (**Supplementary Figure 3a** and **Supplementary Figure 5b**), we next sought to
504 determine whether caspase-1 was activated in D10 melanoma cells upon CTL attack. As shown in
505 **Figure 5e**, D10 cells display a significant and time-dependent increase in caspase-1 activity upon
506 CTL attack, but in a more limited fashion than JY cells (**Figure 2b**), after 5 and 15min conjugation.
507 As with JY cells, caspase-1 activity was often observed in the same cells wherein caspase-3 activity
508 could be detected, although a discreet population of caspase-1-only cells could also be identified
509 (**Figure 5f**).

510 All of these results were consistent with the hypothesis that membrane repair mechanisms acting
511 in melanoma cells to remove perforin pores from the target cell membrane[7,8] might be responsible
512 for dampening perforin-induced caspase activation. To test this concept, we sought to determine
513 the impact of membrane repair on caspase-1 activation. We pre-treated pulsed or non-pulsed D10
514 melanoma cells with either BAPTA-AM, a calcium chelator which inhibits Ca^{2+}-dependent
515 reparative membrane turnover upon perforin pore formation without affecting perforin activity[7,10]
516 or solvent control before conjugating D10 melanoma cells with CTLs for 15min. Consistent with
517 the hypothesis that inhibition of membrane reparative turnover would increase signaling through

518 perforin-dependent pyroptotic pathways, we demonstrated that caspase-1 activity (**Figure 5g**) in
519 pulsed D10 cells was significantly increased upon inhibition of Ca^{2+}-dependent reparative
520 membrane turnover compared to solvent-treated controls.

521

522 *Prolonged interaction with CTLs unveils a delayed apoptotic phenotype in multiple cell types*
523 We next sought to investigate whether the natural depletion of intracellular perforin stores
524 following prolonged interactions between targets and cytotoxic lymphocytes (which has been well-
525 documented[59,91-93]) might inhibit the ability of CTLs to induce pyroptosis during the sustained
526 phase of killing. It is known for both CTLs and NK cells that ultra-rapid perforin/granzyme-
527 mediated killing ultimately gives way to slower complementary killing mechanisms such as death-
528 receptor ligation, which is known to drive apoptosis[91-93]. Thus, we hypothesized that apoptotic
529 target cells may be detectable following longer conjugations. To address this, cell death modality
530 was assessed by Annexin V/PI assay following overnight conjugations of CTLs with four different
531 cell types (**Figure 6a-d**). Under these conditions, a sizeable apoptotic subpopulation of Annexin V
532 single-positive target cells was indeed detectable in all cell lines tested (**Figure 6b**), despite being
533 largely absent from the target cell population at earlier timepoints (**Figure 5b**). This suggests that
534 while the initial wave of perforin-dependent CTL-mediated cell death was lytic and inflammatory,
535 traditional apoptotic cell death mechanisms came into play over time as lytic content became
536 depleted.

537 Collectively, the experiments in this manuscript have demonstrated the engagement of the
538 canonical pyroptotic pathway upon CTL attack in multiple target cell types, downstream of target
539 cell perforation and characterized by K^+ efflux, NLRP3 inflammasome activation, caspase-1
540 activity, and GSDMD activation. The GSDMD pathway was engaged in parallel to the previously

541 described granzyme B-dependent, GSDME-mediated pyroptotic pathway[54,55] during the acute
542 killing phase. Finally, sustained interaction with CTLs unmasked a delayed apoptotic phenotype in
543 the remaining target cells after prolonged conjugations. **Figure 7** illustrates the multi-pronged cell
544 death pathways triggered in target cells upon CTL attack.

545 *Exogenous SMAPs trigger apoptosis*

546 SMAPs are newly described components of the CTL and NK cell lytic arsenal that can serve as
547 autonomous killing entities to annihilate target cells from a distance[4,94,95]. While SMAPs are the
548 subject of intense investigation for their therapeutic potential in cancer patients, their mechanisms
549 of action in killing target cells are still elusive. In particular, the potential of SMAPs to trigger
550 either pyroptotic or apoptotic pathways has not been investigated.

551

552 To investigate SMAP-triggered cell death pathways JY cells were treated with exogenous
553 SMAPs purified from NK-92 cell culture supernatant as described[5]. As shown in **Figure 7a,b**,
554 exposure of JY cells to SMAPs for 4 hours induced only a moderate increase in the proportion of
555 Annexin V^+PI^+ double-positive cells. By contrast, a consistent and significant increase in the
556 Annexin V single-positive population was observed (**Figure 7c**), which is a feature unique to
557 early apoptosis. No increase in PI single-positive cells was observed, confirming that necrotic
558 (non-programmed) cell death did not occur. Together these results are compatible with a SMAP-
559 mediated induction of apoptotic cell death in target cells.

560

561 Collectively, the experiments in this manuscript have demonstrated the engagement of the
562 canonical pyroptotic pathway upon CTL attack in multiple target cell types, downstream of target
563 cell perforation and characterized by K^+ efflux, NLRP3 inflammasome activation, caspase-1

564 activity, and GSDMD activation. The GSDMD pathway was engaged in parallel to the previously
565 described granzyme B-dependent, GSDME-mediated pyroptotic pathway[54,55] during the acute
566 killing phase. Sustained interaction with CTLs unmasked a delayed apoptotic phenotype in the
567 remaining target cells after prolonged conjugations. Conversely exogenous SMAPs triggered the
568 activation of early apoptotic cell death. **Supplementary Figure 17** illustrates the multi-pronged
569 cell death pathways triggered in target cells by the diverse killer cell arsenal.

570

571 **DISCUSSION**

572 In our study we provide two specific mechanistic insights into CTL-mediated target cell death:
573 first, we identified a novel mechanism for the engagement of pyroptotic machinery upon CTL
574 attack, in which perforin itself autonomously engages the caspase-1/GSDMD pyroptotic signaling
575 pathway, and second, we demonstrated that isolated SMAPs fail to activate this pyroptotic pathway
576 in order to induce a distinctly apoptotic cell death phenotype. These observations are consistent
577 with the observed wave of early pyroptotic cell death immediately upon exposure of target cells to
578 CTLs, that eventually gives way to slower apoptotic death in the remaining targets.

579 Our observation that CTLs trigger an initial wave of pyroptotic cell death supports previous studies
580 that postulated a role for pyroptosis upon CTL attack[53-55], and offer a novel mechanism for the
581 engagement of pyroptotic machinery downstream of perforin-mediated pore formation.
582 Conceptually, the pathway we identified links two different perforation events which may
583 cooperate to promote target cell death: the initial perforation of target cells by CTL-derived perforin
584 (which is spatially constrained to the LS and temporally constrained by ultra-rapid synaptic
585 membrane repair mechanisms[7-9]) followed by a more global perforation of target cells by their own

586 endogenous pore-forming gasdermin proteins. Although perforin has been shown to induce
587 osmotic lysis (ie. necrotic non-programmed cell death) at lytic concentrations which is potentiated
588 by blockade of membrane repair mechanisms[10], this is the first report to our knowledge that
589 ascribes a pro-pyroptotic function to perforin, alongside its classical role as a conduit for
590 granzymes. The idea that perforin pore formation can activate the NLRP3/caspase-1/GSDMD
591 pathway is consistent with a well-developed body of literature showing that cytotoxic PFTs,
592 including *Aeromonas hydrophila* -derived aerolysin[22,23], *Vibrio pyarahaemolyticus*-derived
593 thermostable direct hemolysins (TDH)[24], *Staphylococcus aureus*-derived Paton-Valentine
594 leukocidin (PVL)[26], *Trueperella pyogenes*-derived pyolysin (PLO)[27] and *S. aureus*-derived α-
595 hemolysin[22,25], trigger caspase-1 activation in perforated cells via the NLRP3 inflammasome. The
596 pores formed from these bacterial toxins are almost universally permeable to K^+ (reviewed in[18]),
597 and not surprisingly, NLRP3/caspase-1 activation in these contexts is often K^+ efflux-dependent[22-
598 27]. Thus, perforin functionally mimics the activity of the ancestral pore-forming bacterial toxins
599 described above, demonstrating that this ancient attack mechanism retains utility in the human CTL
600 arsenal today. This may be advantageous for CTLs attempting to circumvent granzyme-specific
601 resistance mechanisms, such as the serine protease inhibitors (**serpins**), which have been shown to
602 confer resistance to both chimeric antigen receptor (**CAR**) T cells and immune checkpoint
603 blockade (**ICB**) therapy[96,97]. As such, engineering immunotherapies that potentiate perforin-
604 activated pyroptotic signaling pathways may be a useful complementary approach. Of note, loss of
605 intracellular potassium homeostasis downstream of membrane perforation by bacterial PFTs has
606 also been suggested to trigger other adaptations in addition to inflammasome activation (including
607 arrest of protein synthesis, activation of the mitogen-activated protein kinase (MAPK) pathway,
608 and induction of autophagy)[18,98]; the extent to which such downstream responses occur upon

609 perforin pore formation in tumor cells, and if so whether they ultimately enhance or attenuate CTL
610 cytotoxicity, remains to be determined.

611 Although SMAPs have been shown to contain significant quantities of perforin, it and other
612 cytotoxic molecules are understood to be largely encapsulated within the SMAP's impermeable
613 glycoprotein shell[4]. This shell may prevent soluble perforin from encountering the target cell
614 membrane, thus limiting the crucial perforation step that leads to the K^+ efflux and inflammasome
615 activation and encouraging a slower apoptotic form of cell death. Whether the alternative
616 pyroptotic GSDME pathway is not triggered by SMAPs that contain granzyme B is presently
617 elusive. It is tempting to speculate that since the uptake of SMAPs by target cells should not occur
618 via perforin pores, but rather be mediated by the endocytic compartment as we observed in
619 CTL/target cell conjugates[99], the SMAP-associated granzyme B might trigger a different death
620 cascade than that triggered by the perforin-dependent cytosolic granzyme B.

621 We and others have shown that ultra-rapid Ca^{2+}-dependent membrane repair is a vital resistance
622 mechanism against CTL attack[7-10]. Our current data implies that K^+-dependent pro-death signalling
623 may be initiated by the same perforation event as Ca^{2+}-dependent pro-survival repair mechanisms.
624 Previous studies by ourselves and others have shown that BAPTA-AM-mediated inhibition of
625 Ca^{2+}-dependent synaptic membrane repair results in an overt increase in target cell death in
626 response to either perforin exposure or CTL attack[7,10], and the current study suggests that
627 promotion of caspase-1-dependent pyroptosis may be one mechanism by which this occurs.
628 Importantly, Ca^{2+}-dependent membrane repair mechanisms also facilitate the removal of
629 gasdermin pores from the plasma membrane[39,40], and thus inhibition of membrane repair might be
630 a doubly effective strategy for promoting both effective target perforation by perforin and
631 ultimately gasdermin-mediated cell death.

632 Of note, Ca^{2+} flux has also been proposed as a common mediator of NLRP3 inflammasome
633 activation[21,100], but in this study, chelation of intracellular Ca^{2+} with BAPTA-AM in D10
634 melanoma cells increased caspase-1 activation, suggesting that inflammasome activation in this
635 system is not dependent on Ca^{2+} flux.

636 As mentioned above, the effect of siRNA-mediated NLRP3 inhibition on caspase-1 activity was
637 modest in this system, and this observation is consistent with the presence of multiple other
638 inflammasomes which may promote caspase-1 activation upon CTL attack[101]. Concurrent
639 activation of other inflammasome sensors in combination with NLRP3 is well-documented
640 (reviewed in [21]) and NLRC4 in particular has been shown to be activated alongside NLRP3 upon
641 membrane perforation by bacterial PFTs[24]. Likewise, NLRP1 can be activated upon disruption of
642 intracellular K^+ homeostasis[68] and may serve as an additional platform for caspase-1 activation in
643 our system. In addition to detecting loss of intracellular K^+, inflammasome sensors also collectively
644 detect a diverse array of danger signals (including abnormal protease activity, abnormal
645 localization of nucleic acids, mitochondrial dysfunction, ROS production, disruption of the actin
646 cytoskeleton, ribotoxic stress, and others)[101]. Many of these intracellular danger signals are present
647 upon CTL attack[3], which may firstly ensure vigorous and continuous caspase-1 activation in the
648 presence of continued danger and secondly make the activation of caspase-1 relatively robust to
649 the depletion of an individual inflammasome sensor (such as NLRP3). Nonetheless, the results of
650 our study align with a previous report that showed that antigen-dependent CTL feedback can induce
651 NLRP3-dependent caspase-1 activation in antigen-presenting cells (**APCs**) through a perforin-
652 dependent and K^+ -dependent mechanism, although these interactions were non-lethal and instead
653 led to sustained IL-1β secretion by viable APCs[102].

654 In this study, we provide evidence that caspase-1 is activated upon human CTL attack, as well as
655 upon exposure of target cells to recombinant human perforin (**Figure 2**). In addition to promoting
656 GSDMD-mediated pyroptosis, caspase-1 activation may have additional downstream
657 consequences; proteomics studies have revealed dozens of substrates for caspase-1, including
658 cytoskeletal proteins, chaperone proteins (including heat shock proteins), and trafficking proteins
659 (such as RAB7), as well as cytokines (pro-IL1β and pro-IL-18) and a notable constellation of
660 proteins involved in glycolysis[103,104]. Although GSDMD is thought to be cleaved the fastest[103], this
661 does not preclude a role for other caspase-1 substrates in the target cell response to CTL attack,
662 which may become particularly relevant in the context of prolonged or sub-lethal encounters.
663 Further studies will be necessary to elucidate other functions of caspase-1 prior to induction of
664 CTL-driven pyroptosis.

665 Building upon previous studies of GSDME-mediated pyroptosis upon CTL attack[54,55], we also
666 provide evidence in this study that concurrent inhibition of both GSDMD and GSDME diminishes
667 specific killing upon CTL attack, despite robust caspase-1 and -3 activation (**Supplementary**
668 **Figure 16**). This suggests that caspase-1 and -3 activity alone is insufficient to achieve fast, optimal
669 perforin/granzyme-mediated cytotoxicity and supports a role for gasdermins as the final
670 executioners of target cell death. A multi-pronged approach in which both GSDMD and GSDME
671 are activated upon CTL attack would be particularly important in transformed cells wherein
672 individual gasdermins can be functionally inhibited through repression, inactivation, or mutation
673 (reviewed in [3,47,105]). Thus, activation of multiple pyroptotic pathways upon CTL attack would
674 increase the probability of successfully circumventing such resistance mechanisms. The evolution
675 of multiple gasdermins has been speculated to serve precisely this purpose, offering multiple
676 redundant or partially redundant cell death pathways that are activated during cellular stress[28].

677 More globally, the initiation of pyroptotic signaling pathways may be particularly vital in
678 transformed cells wherein apoptotic pathways are inhibited, while induction of apoptosis by
679 SMAPs may be crucial in transformed cells whose pyroptotic pathways are inhibited. Thus, the
680 activation of two pyroptotic pathways (by perforin and granzyme respectively) upon CTL attack
681 offers functional redundancy to circumvent inhibition of individual pyroptotic pathways, whereas
682 the activation of an apoptotic pathway by SMAPs offers more global redundancy in the context of
683 dual inhibition of both pyroptotic pathways.

684 Typically, plasma membrane permeabilization during pyroptosis is considered the main
685 mechanisms of gasdermin-mediated toxicity; however, gasdermins have been shown to target other
686 organelles enriched in cardiolipins, including lysosomes and mitochondria[80,106], causing
687 mitochondrial depolarization, disruption of the mitochondrial network, release of mtDNA and
688 mitochondrial proteins, and lysosome deacidification/decay, which ultimately lead to a failure of
689 cell viability prior to PMR[80,107] (reviewed in [35]). Although we observed PMR in target cells in our
690 system using live-cell imaging (**Figure 4**), the extent to which intracellular gasdermin-mediated
691 injures contribute to target cell demise prior to lysis remains to be characterized.

692 Despite the aforementioned publications demonstrating roles for GSDME and GSDMB in CTL-
693 mediated pyroptosis[53-55], the notion that CTL attack activates pyroptosis remains controversial
694 within the field. Historically, apoptosis was the only well-recognized form of RCD in the literature
695 and thus the notion that CTLs killed by apoptosis became a well-established paradigm. In this
696 study, we provide evidence for activation of caspase-1/GSDMD upon CTL attack and demonstrate
697 that cytotoxicity of antigen-specific human CTLs is functionally diminished through either siRNA-
698 mediated inhibition of GSDMD and GSDME expression or Crispr Cas9-mediated *GSDMD* and
699 *GSDME* knockout in target cells, providing proof-of-principle that target cells are capable of dying

700 by pyroptosis under the conditions of this study. Although these results do not suggest that the
701 majority of CTL-driven cytotoxicity events across all species, diseases, and contexts is pyroptotic
702 in nature, they do provide ample rationale for considering pyroptosis as a viable alternative
703 mechanism for perforin/granzyme-mediated target cell death. Our results are consistent not only
704 with the recent studies directly implicating pyroptosis in perforin/granyzme-mediated killing[53-55],
705 but also with a number of earlier studies that highlighted non-apoptotic and/or immunogenic cell
706 death modalities upon CTL attack[48-52]. Collectively, these studies involve a number of different
707 contexts, across both mouse and human model systems, *in vitro* and *in vivo*, illustrating that our
708 experimental conditions are not unique in promoting pyroptotic cell death upon CTL attack. At the
709 same time, our observation of a SMAP-mediated apoptotic phenotype highlights another
710 mechanism by which observations of apoptotic cell death and pyroptotic cell death across different
711 study conditions may be reconciled.

712 Further to this, it is worth emphasizing that cell death modality upon CTL attack is almost certainly
713 context-dependent. On the CTL side, even clonal human CTLs are phenotypically and functionally
714 heterogeneous, with notable differences in the expression of cytotoxic molecules such as perforin
715 and granzymes across clonal populations[108-111]. Given that different classes of cytotoxic molecules
716 have discrete biological functions, the effect of a given CTL on a target cell may depend at least
717 partially upon its individual cytotoxic payload. CTLs subpopulations with high perforin expression
718 but relatively low expression of granzymes have been observed[110,111] and these cells may indeed
719 be endowed with perforin-dependent, granzyme-independent cytotoxic mechanisms; conversely,
720 CTLs with lower perforin expression may preferentially induce killing through a SMAP-mediated
721 apoptotic pathway. Indeed it has previously been shown that the presence or absence of certain
722 lytic molecules can change not just the extent but also the modality of CTL-mediated killing[50], with

723 CTLs deficient in both granzyme A and B inducing a non-apoptotic PCD modality characterized
724 by swelling, membrane rupture, and simultaneous onset of PI uptake with Annexin V staining[50].
725 As such, it stands to reason that CTL-intrinsic factors play a role in determining target cell death
726 modality. Further live-cell imaging studies could reveal at the single-cell level whether individual
727 CTLs preferentially induce a specific cell death modality, or whether individual CTLs trigger
728 different cell death modalities as a result of different cytotoxic mechanisms engaged sequentially
729 during serial killing (as has been proposed for NK cells[93], reviewed herein[112]).

730 On the target cell side, cancer cells are highly heterogeneous, both at the intra-tumoral and inter-
731 tumoral level, in terms of differentiation state, gene expression profile, mutational burden, presence
732 or absence of viral genomic integration, epigenetic modifications, and ultimately functional
733 behaviour[113]. This heterogeneity, particularly as it pertains to the dysregulation of cell death
734 machinery, likely plays a large role in determining cell death modality. Dysregulation of apoptotic
735 circuitry specifically was one of the six foundational hallmarks of cancer identified by Hanahan
736 and Weinberg[114] and resistance to cell death through mutation, suppression, or dysregulation of
737 cell death machinery (both apoptotic and pyroptotic) continues to be considered a defining
738 characteristic to the present day and major functional obstacle to CTL-mediated therapies[3,115,116].
739 The integration of viral genomes into cancer cells (particularly EBV, hepatitis B and human
740 papilloma virus)[117] may introduce an additional level of cell death suppression through specific
741 virally encoded modulators of cell death pathways. Thus, since an attacking CTL may face a
742 transformed target wherein one or more cell death pathways have been rendered functionally
743 impotent, the apoptosis-versus-pyroptosis decision balance is influenced by which cell death
744 pathways still retain functionality following oncogenic transformation. Because multiple cell death
745 pathways are initiated in parallel by an attacking CTL, it would not be unexpected that dying targets

746 likewise display characteristics of multiple cell death modalities; some of these signaling pathways
747 may be prematurely terminated due to the mutation, suppression, or inactivation of key
748 components, while others may be actively involved in executing the cell death decision. The
749 presence or absence of membrane repair mechanisms might also affect cell death modality, and
750 indeed there is precedent in the literature to suggest that reparative membrane turnover promotes a
751 slower, apoptotic cell death modality whereas inhibition of these Ca^{2+}-dependent repair
752 mechanisms unleashes a fast, lytic, and non-apoptotic cell death modality following target
753 perforation[10]. For all of these reasons, cell death modality upon CTL attack is likely to be context-
754 dependent and may not fit neatly into a single well-described PCD modality due to the multi-
755 pronged nature of CTL attack.

756 In the context of oncology, multiple chemotherapeutics[29,118,119], small molecule inhibitors[120],
757 radiation[121-123], and tumor immunotherapy[53,55] as well as nanoparticle-based approaches for
758 therapeutic delivery of gasdermins[39,124] have been shown to drive tumor cell pyroptosis, which
759 strongly favours anti-tumor immunity and tumor clearance, particularly in the context of turning
760 "cold" tumors "hot" (reviewed in [105,125]). Mass spectrometry-based human proteomics studies have
761 revealed that GSDMD-mediated pyroptosis releases several hundred different proteins, through a
762 combination of conventional secretion, unconventional secretion, vesicle/lysosome release, and
763 passive cell lysis (e.g. LDH)[126]. The pyroptotic secretome is particularly enriched in DAMPs (e.g,
764 HMGB1, galectins, S100 family proteins, and lysosomal cathepsins) which collectively serve as
765 potent proinflammatory danger signals in the extracellular environment, through various
766 mechanisms including direct TLR ligation[126]. Activation of local inflammatory signaling cascades
767 by the pyroptotic secretome potentiates anti-tumor immunity by acting on multiple steps of the
768 cancer-immunity cycle[127], including enhanced antigen presentation, priming of APCs, and immune

769 infiltration, as reviewed elsewhere[105,125]. In addition, recent studies have suggested that the
770 pyroptotic corpse itself may be directly immunogenic due to "crowning" of the corpse by F-actin-
771 rich filopodia that engage the F-actin receptor CLEC9A on dendritic cells and promote engagement
772 of the adaptive immune system[128]. As such, our results fit within a mature field of literature that
773 has repeatedly highlighted how pyroptotic cell death can serve as a bridge between inflammation
774 and adaptive immunity.

775 Nonetheless, the inflammation induced by pyroptosis is a double-edged sword, which has been
776 associated with tumorigenesis[105] as well as adverse inflammatory side effects including cytokine
777 release syndrome[55,129] and certain side-effects of chemotherapeutics[29]. Since cell death modality is
778 known to have such a profound impact on treatment efficacy and side effect profile, one can
779 envision there would be clinical utility in delineating how given CTL-mediated immunotherapies
780 induce cell death. Given that expression of gasdermin family proteins is heterogeneous both within
781 and between tumor types (reviewed in [47,105]), it is conceivable that individual tumors have a pre-
782 existing "fingerprint" of gene expression which sensitizes them to different cell death modalities
783 and may impact efficacy and side effect profile of CTL-mediated therapies. Depending upon
784 whether it is clinically advisable to promote or inhibit inflammatory cell death, different
785 combination therapies could be envisioned that are designed to enhance or prevent pyroptosis.
786 Proof of concept for this has already been demonstrated with chemotherapeutics, wherein the
787 methyltransferase inhibitor decitabine enhanced GSDME expression and promoted pyroptosis
788 following nanoparticle-mediated delivery of cisplatin[118].

789 In the context of CTL-mediated immune surveillance against cancer, the observation that perforin
790 and SMAPs trigger pyroptosis and apoptosis respectively is intriguing. While perforin-mediated
791 cell death might serve as immunogenic cell death (**ICD**), important to trigger and amplify immune

792 response, SMAP-induced apoptosis might serve as a source of tumor antigens for cross-priming.
793 Accordingly, SMAPs contain CCL5 and XCL2 that are chemoattractants of cDC1, the key DC
794 subtype responsible for cross-priming anti-tumor $CD8^+$ T cells[4,130]. It is tempting to speculate that
795 the parallel activation of perforin-mediated pyroptosis in some tumor cells and of SMAP-mediated
796 apoptosis in other cells might alert the immune system while ensuring antigen presentation,
797 resulting in sustained and efficient immune responses. Harnessing the apoptotic/pyroptotic cell
798 death balance in cancer patients might become a novel and interesting path to follow in the
799 development of immunotherapeutic strategies against cancer.

800 Outside the context of tumor immunology, understanding whether CTLs and/or CTL-derived
801 perforin can trigger target cell or bystander cell pyroptosis may be crucially important for
802 neuroinflammatory conditions (such as multiple sclerosis[85,131]), autoimmune disease, and chronic
803 infection, wherein canonical GSDMD-dependent pyroptosis has been implicated as a driver of
804 chronic inflammation[47,132,133]. In such conditions, the inflammatory pyroptotic secretome
805 perpetuates bystander tissue damage, leading to a feed-forward cycle of tissue damage and
806 inflammation[47,132]; as such, understanding and preventing CTL-driven pyroptosis may be a widely
807 applicable therapeutic approach. Perforin itself has been identified as a driver of tissue damage in
808 chronic viral infections, and its inhibition has quantifiable protective effects in various models[134].

809 In conclusion, our study provides evidence that perforin-mediated pore formation at the LS leads
810 to potassium efflux, triggering a proinflammatory NLRP3/caspase-1/GSDMD pyroptotic signaling
811 cascade. We propose a novel pro-pyroptotic function for perforin, which is consistent with the role
812 of prokaryotic pore-forming toxins and expands its cytotoxic role beyond that of a simple conduit
813 for granzymes. Conversely, we show that SMAPs preferentially trigger apoptosis, thus providing
814 a complementary source of antigens for anti-tumor immune responses. Our results highlight a novel

815 mechanism for the engagement of pyroptotic machinery upon CTL attack and highlight the
816 complexity and diversity of the human CTL lytic arsenal.

METHODS

Cell Culture

Cell culture was performed as previously described[7,8]. Human $CD8^+$ T cells were purified from healthy donor blood samples using the RosetteSep Human $CD8^+$ T Cell Enrichment Cocktail (StemCell Technologies). For cloning, HLA-A2-restricted $CD8^+$ T cells specific for the NLVPMVATV peptide of the cytomegalovirus protein pp65 were single-cell sorted into 96-U-bottom plates using a BD FACSAria II cell sorter using tetramer staining. Cells were cultured in RPMI 1640 medium supplemented with 5% human AB serum (Inst. Biotechnologies J.BOY), 50µmol/L 2-mercaptoethanol, 10mM HEPES, 1X MEM NEAA (Gibco), 1X Sodium pyruvate (Sigma), 10µg/ml ciprofloxacine (AppliChem), 100 IU/ml human rIL-2 and 50 ng/ml human rIL-15 (Miltenyi). $CD8^+$ T-cell clones were stimulated in complete RPMI/HS medium containing 1 µg/ml PHA with 1 x 10^6 per ml 35 Gy irradiated allogeneic peripheral blood mononuclear cells (isolated on FicollPaque Gradient from blood of healthy donors). Clones were restimulated every 2 weeks. Blood samples were collected and processed following standard ethical procedures after obtaining written informed consent from each donor and approval by the French Ministry of Research (transfer agreement AC-2020-3971). Approbation by the ethical department of the French Ministry of the Research for the preparation and conservation of cell lines and clones starting from healthy donor human blood samples has been obtained (authorization no. DC-2021-4673). Approbation by the ethical department of the French Ministry of the Research for the preparation and conservation of cell lines issued from cancer patients' tissue samples has been obtained (authorization N° DC-2021-4673) and written informed consent was obtained from each donor.

EBV-transformed B cells (JY) HLA-$A2^+$ were used as sensitive target cells. D10 HLA-$A2^+$ human melanoma cells were kindly provided by Dr G. Spagnoli, Basel, Switzerland. LB2259-MEL.A

840 HLA-A2$^+$ human melanoma cells were kindly provided by Dr P. Coulie and N.V. Baren, Brussels,
841 Belgium. TouM3 cells were isolated in-house from primary melanomas, which were first
842 dissociated using the Human Tumor Dissociation Kit (MiltenyiBiotec) on the GentleMACS
843 Dissociator. Total cells were then filtered on a 70µm filter (BD Falcon) and red blood cells
844 eliminated by ACK treatment. Tumor-infiltrating lymphocytes (**TILs**) were removed by positive
845 selection using a TIL Isolation Kit (MiltenyiBiotec) by magnetic separation (LS Column) and
846 the negative fraction of this separation (corresponding to retained cells) was incubated with
847 magnetic beads from the Tumor Cells Isolation Kit (MiltenyiBiotec) and separated by magnetic
848 sorting using LS column. After isolation, melanoma cells were cultured in T25cm^2 flasks for
849 several days and amplified twice before freezing (FCS/90%DMSO).

850 All target cells were cultured in RPMI 1640 GlutaMAX supplemented with 10% FCS and
851 50µmol/L 2-mercaptoethanol, 10mM HEPES, 1X MEM NEAA (Gibco), 1X Sodium pyruvate
852 (Sigma), 10µg/ml ciprofloxacine (AppliChem). All cell lines were screened biweekly for
853 mycoplasma contamination using MycoAlert mycoplasma detection kit (Lonza). Melanoma and
854 JY cells were subjected to cell line typing (Microsynth Ecogenics, Switzerland) to authenticate
855 their identity and ensure that no contamination of human origin was detectable.

856

857 **Drug treatments**

858 To induce pyroptosis, cells were plated at a density of 2.5 x 10^4 cells per well in a 96-well plate,
859 treated with 100µM nigericin (CliniSciences #ICT-6698 or Invivogen #tlrl-nig) and incubated at
860 37°C and 5% CO_2 for the indicated time (2hr unless otherwise indicated). This high concentration
861 of nigericin was utilized to ensure that the majority of cells underwent swift and definitive
862 pyroptosis and to circumvent the need for an LPS-priming step. To induce apoptosis, cells were

863 plated using the same conditions and treated with 6.6µM staurosporine (*Streptomyces*) (InSolution,
864 Merck #569396) and incubated at 37°C and 5% CO_2 for the indicated time.

865 To assess the effect of Ca^{2+} chelation in target cells on pyroptotic signaling pathways, target cells
866 were treated with 50µM BAPTA-AM for 2hr at 37°C (ThermoFisher Scientific, #B6769) and
867 thoroughly washed before conjugation with CTLs.

868 To test the effect of CTL lytic granule depletion, CTLs were pre-treated with monensin
869 (FisherScientific GolgiStop™ containing 0.26% monensin, diluted 1:1000, #BDB554724) for 2hr
870 at 37°C and thoroughly washed before conjugation with targets.

871 To assess the effects of caspase-1 inhibition, targets were pre-treated for 2hr with 100µM VX-765
872 (InvivoGen, #inh-vx765) during the 2hr antigen pulse step and washed prior to conjugation with
873 CTLs.

874 **Annexin V/PI Apoptosis Detection**

875 Target cells (JY and D10) were either non-pulsed or pulsed with 10µM CMV p65 antigenic peptide
876 for 2hr at 37°C and 5% CO_2, washed and transferred to a 96-well U-bottom plate at 1 x 10^4 cells
877 per 100µl RPMI 5% FCS/HEPES. CTL were previously stained with CellTrace™ Violet
878 (ThermoFisher Scientific, #C34557) for 30min at 37°C and 5% CO_2, washed and added to the
879 target cells at an effector:target ratio of 4:1 in 100µl RPMI 5% FCS/HEPES. Plates containing
880 samples were spun for 1min and incubated at 37°C and 5% CO_2 for either 1 or 4hr. At the endpoint,
881 cells were spun, washed in ice cold PBS, and assayed for Annexin V and PI staining according to
882 manufacturer's instructions (BD Pharmingen FITC Annexin V Apoptosis Detection Kit I,
883 #AB_2869082). In a subset of experiments, CTLs were treated with monensin (BD GolgiStop™;
884 #51-2092KZ) at a dilution of 1:1000 for 2hr and washed thoroughly prior to conjugation with

885 targets. Samples were acquired using the MACSQuant Analyzer 10 flow cytometer (Miltenyi
886 Biotec) and analyzed using FlowJo 10.

887 For drug controls, target cells were plated at a density of 2.5 x 10^4 cells per well in a 96-well U-
888 bottom plate, incubated with either nigericin (pyroptosis control), staurosporine (apoptosis
889 control), or solvent controls for the indicated time, and subjected to Annexin V and PI staining as
890 described above.

891 **Lactate Dehydrogenase Supernatant Activity Assay**

892 Target cells (JY and D10) were either non-pulsed or pulsed with 10µM CMV p65 antigenic peptide
893 for 2hr at 37°C and 5% CO_2, washed and transferred to a 96-well U-bottom plate at 1 x 10^4 cells
894 per 100µl RPMI 5% FCS/HEPES. CTL were added to the target cells at an effector:target ratio of
895 4:1 in 100µl RPMI 5% FCS/HEPES. Plates containing samples were spun for 1min and incubated
896 at 37°C and 5% CO_2 for 4hr. At the endpoint, cells were spun and supernatant removed for storage
897 at -20°C and then analyzed using the CytoSelect™ LDH Cytotoxicity Assay Kit (Cell Biolabs Inc,
898 #CBA-241) according to manufacturer's instructions. Absorbance (optical density at 450nm) was
899 assessed using a CLARIOstar plate reader (BMG Labtech), with background subtracted (optimal
900 density at 650nm).

901 As a positive control, JY and D10 target cells were plated at a density of 2.5 x 10^4 cells per well in
902 a 96-well U-bottom plate and incubated with 100µM nigericin or solvent controls for 2hr.
903 Supernatants were harvested and subjected to LDH detection as described above.

904

905 **HMGB1 Immunoassay**

906 Target cells (JY and D10) were either non-pulsed or pulsed with 10µM CMV p65 antigenic peptide
907 for 2hr at 37°C and 5% CO_2, washed and transferred to a 96-well U-bottom plate at 2.5 x 10^4 cells

908 per 100µl RPMI 5% FCS/HEPES. CTL were added to the target cells at an effector:target ratio of
909 4:1 in 100µl RPMI 5% FCS/HEPES. Plates containing samples were spun for 1min and incubated
910 at 37°C and 5% CO_2 for 1hr. At the endpoint, supernatant was removed for immediate analysis
911 using the LumitTM HMGB1 (Human/Mouse) Immunoassay (Promega, #W6110). Luminescent
912 samples were read in opaque white 96-well plates using a CLARIOstar plate reader (BMG
913 Labtech).

914 As a positive control, JY and D10 target cells were plated at a density of 2.5 x 10^4 cells per well in
915 a 96-well U-bottom plate and incubated with 100µM nigericin or solvent controls for 2hr.
916 Supernatants were harvested and subjected to HMGB1 assay as described above.

917 **Caspase-1 and Caspase-3 Activity-Dependent Fluorescent Assays**

918 Target cells were either non-pulsed or pulsed with 10µM CMV p65 antigenic peptide unless
919 otherwise indicated for 2hr at 37°C and 5% CO_2, washed and transferred to a 96-well U-bottom
920 plate at 1 x 10^4 cells per 100µl RPMI 5% FCS/HEPES. Plated target cells were single-or double-
921 stained with either far-red fluorescent FLICA 660 Caspase-1 (YVAD) reagent (ImmunoChemsitry,
922 #9122) or green fluorescent FAM-FLICA Caspase-3/7 (DEVD; detects active form of both
923 caspase-3 and -7) reagent (ImmunoChemsitry, #93), according to manufacturer's instructions for
924 20min at 37°C and 5% CO_2. CTL were stained with CellTrace™ Violet (ThermoFisher Scientific,
925 #C34557) for 30min at 37°C and 5% CO_2, washed and added to the target cells at an effector:target
926 ratio of 4:1 unless otherwise indicated in 100µl RPMI 5% FCS/HEPES. Plates containing samples
927 were spun for 1min and incubated at 37°C and 5% CO_2 for either 5 or 15min. At the endpoint, cells
928 were washed, fixed with the provided fixative (ImmunoChemistry #636), and stored at 4°C before
929 being acquired using the MACSQuant Analyzer 10 flow cytometer (Miltenyi Biotec) and analyzed
930 using FlowJo 10. In a subset of experiments, CTLs were treated with monensin (BD GolgiStop™;

931 #51-2092KZ) at a dilution of 1:1000 for 2hr and washed thoroughly prior to conjugation with
932 targets.

933 As a positive control, JY and D10 target cells were plated at a density of 2.5 x 10^4 cells per well in
934 a 96-well U-bottom plate and incubated with 100µM nigericin or solvent controls for 2hr, before
935 being stained with FLICA 660 Caspase-1 (YVAD) reagent for 20 mins and analyzed as described
936 above.

937

938 **Transfection of Target Cells**

939 From 8 x 10^5 to 1x 10^6 JY cells were washed and resuspended in 100µl OPTI-MEM and transferred
940 in electroporation cuvettes (0.2cm). 200 pmoles of each different siRNA targeting mRNA coding
941 for *GSDMD*, *GSDME*, *CASP1*, *NLRP3*, or non-targeting siRNA were added in the cell suspension.
942 After electroporation at 160V during 10 ms (500µF) with a exponential waveform using the Gene
943 PulserXcell Electroporation systems (Bio-rad), transfected JY cells were seeded in pre-warmed
944 culture medium and used for experiments 24-48h after electroporation. Transfection efficiency was
945 evaluated by qPCR or immunoblot.

946

Target	siRNA Sequence (5'->3')
GSDMD	s36339 : GGAACUCGCUAUCCCUGUUtt s36340 : CGUGAGUGUGGACCCUAAtt s36341 : AGCUGGUUAUUGACUCUGAtt
GSDME	S230618 : GAGAGAACAAUAAAUCUGAtt S4065 : GGAUGGACCAUUAAGUGUUtt S4066 : GAAAGAUACAGAAAGGUUUtt
NLRP3	s41554 : GGAGAGACCUUUAUGAGAAtt s41555 : GCUUUGUCCUCGGUACUCAtt s41556 : GCACGUGUUUCGAAUCCCAtt
CASP1	s2407 : GGAAGACUCAUUGAACAUAtt s2408 : CCACUGAAAGAGUGACUUUtt s2409 : UGGAGGAAAUUUUCCGCAAtt
Non-targeting	4390843 (proprietary sequence) 4390846 (proprietary sequence)

947

948 **Generation of GSDMD and GSDME Knock-out JY cells**

949 GSDMD/E double knock-out JY cells were generated by electroporation of ribonucleoprotein
950 complex sgRNA/Cas9 in JY cells using the Neon transfection system (Thermo Fisher). Briefly,
951 1×10^6 JY cells were resuspended in 10 µL of R buffer, mixed with 240 ng of sgRNA for GSDMD,
952 240 ng of sgRNA for GSDME and 2 µg of HiFi Cas9 endonuclease creating a functional editing
953 RNP complex (ordered from IDT) and electroporated using a 10 µL electroporation pipette tip with
954 two 30 ms pulses at a voltage of 1100 V. Cells were then dispensed directly into a 6-well plate
955 containing 3 mL of R10 cell medium without antibiotic and cultured for 3–5 days before assessing
956 bulk KO efficiency by qPCR. To generate negative control cell lines, JY cells were transfected
957 using non-targeting sgRNA and HiFi Cas9 endonuclease under identical conditions.

958

959 **Potassium Efflux Assays**

960 To assess the relative intracellular concentration of K^+ upon target cell perforation, JY cells were
961 non-pulsed or pulsed with 10µM antigenic peptide (CMV p65) for 2hr at 37° and 5% CO_2, washed,
962 and loaded with 2.5 µM Ion Potassium Green-2 AM (Abcam, ab142806) for 30min. Stained JY
963 cells were then conjugated with antigen-specific CTLs at the indicated effector:target ratios for 5
964 and 15min, stained with viability dye (eFluor 450) and subjected to analysis by flow cytometry.
965 Samples were acquired using the MACSQuant Analyzer 10 or MACS Quant Analyzer VYB flow
966 cytometers (Miltenyi Biotec) and analyzed using FlowJo 10.

967 As a positive control, JY cells were plated in 96-well U-bottom plates at a density of 2.5 x 10^4
968 cells/well and treated with the K^+ ionphore nigericin (100µM) at time points ranging from 1min to
969 2hr, before being stained with IPG-2 AM and viability dye and analyzed as above.

970

971 **Exogenous Perforin Experiments**

972 JY target cells were plated in 96-well U-bottom plates at a density of 2.5 x 10^4 cells/well in perforin
973 binding buffer to facilitate perforin phospholipid binding (20mM HEPES, 150nM NaCl, 2.5mM
974 $CaCl_2$). Recombinant human perforin-1 (AA 22-555, Enzo Life Science ENZ-PRT313-0200) was
975 added at the indicated concentrations for a duration of 15min, after which cells were spun, washed,
976 and re-suspended for analysis by flow cytometry. In experiments with excess extracellular K^+, the
977 perforin binding buffer above was replaced with buffer containing KCl (20mM HEPES, 150nM
978 NaCl, 2.5mM $CaCl_2$).

979 To assess intracellular K^+ concentration, JY cells were plated in 96-well U-bottom plates at a
980 density of 2.5 x 10^4 cells/well in perforin binding buffer and stained with the fluorescent K^+ probe,
981 Ion Potassium Green-2 AM for 30min as described above. Recombinant perforin was added at a
982 concentration of 4 or 8µg/mL for 5 and 15min, after which cells were spun, washed and analyzed
983 by flow cytometry.

984 To assess caspase-1 activation, JY cells were plated in 96-well U-bottom plates at a density of 2.5
985 x 10^4 cells/well in perforin binding buffer and pre-loaded with far-red caspase-1 activity-dependent
986 probe (ImmunoChemsitry, #9122). Recombinant perforin was added at a concentration of 8µg/mL
987 for 30min, after which cells were spun, washed, and fixed with the provided fixative
988 (ImmunoChemistry #636), prior to analysis by flow cytometry.

989 For Annexin V/PI assays, JY cells were plated in 96-well U-bottom plates at a density of 2.5 x 10^4
990 cells/well in perforin binding buffer and recombinant perforin added at a concentration of 8µg/mL
991 for 60min, after which cells were washed and subjected to Annexin V/PI staining as described

992 above (BD Pharmingen FITC Annexin V Apoptosis Detection Kit I, #AB_2869082) before
993 analysis by flow cytometry.

994 **Real-time quantitative PCR**

995

996 Isolation of RNA was performed using the Quick-RNA mini Prep kit (ZymoResearch) and RNA
997 concentration was assessed with the NanoDrop 1000 system (Thermo Scientific). cDNA was
998 synthesized using the SuperScript™ IV VILO™ (SSIV VILO) Master Mix (Invitrogen).

999 The gene expression of *GSDMA-E*, *CASP1* and *NLRP3* was evaluated by real-time quantitative
1000 (RTqPCR) using TaqMan gene expression assays (Applied Biosystems) according to
1001 manufacturer's recommendations, using a StepOne Real-Time PCR System (Applied Biosysrems).
1002 All reactions were performed in triplicates and relative gene expression levels were evaluated using
1003 the comparative CT (threshold cycle) method (2-deltaCT). GAPDH was used as endogenous
1004 controls for normalization.

Target	Sequence
GSDMA	Hs00403267_m1
GSDMB	Hs00218565_m1
GSDMC	Hs00937071_m1
GSDMD	Hs00986748_g1
GSDME	Hs00903185_m1
NLRP3	Hs00918082_m1
CASP1	Hs00354836_m1

GAPDH	Hs99999905_m1

1005

1006

1007 **Immunoblot**

1008 *Sample collection:* To assess baseline expression of pyroptosis proteins (GSDMD, GSDME,
1009 NLRP3 and caspase-1), 2.5 x 10^6 JY, D10, or MDA-MB231 cells were washed in cold PBS and
1010 resuspended in RIPA buffer with cOmplete^{TM} protease inhibitor cocktail (Sigma-Aldrich).

1011 *Protein extraction and immunoblot:* After 15min on ice with agitation every 5min, extracts were
1012 centrifuged to pellet DNA and the supernatant was collected. Proteins were quantified by Pierce
1013 BCA protein assay kit (Thermo Fisher Scientific) according to manufacturer's instructions.
1014 Proteins were then denatured in Laemli buffer (5min at 95° with agitation). 15µg of protein was
1015 loaded for each sample in precast 4-15% Mini-Protean TGX Stain-Free 30µl 10-well
1016 polyacrylamide gels (Bio-Rad #456803) along with Kaleidoscop protein ladder (Bio-Rad). Gels
1017 were run and blotted onto a nitrocellulose membrane and blocked with 3% non-fat dry milk in Tris-
1018 buffered saline with Tween (TBST) for 1hr. Membrane was incubated with the indicated primary
1019 antibodies overnight at 4°C with agitation, followed by 1hr incubation with the corresponding
1020 HRP-tagged secondary antibodies. Blots were developed using ECL Clarity (Max) detection
1021 reagent (Bio-Rad) and imaged using ChemiDoc MP System (Bio-Rad).

1022

1023

1024 **Primary Antibodies**

Target	Application	Isotype	Supplier	Identifier	Dilution
GSDMD (*total*)	WB/IF	Mouse IgG1	Sigma	Clone 3F12-1B2 #WH0079792M1	WB: 1/200 IF: 1/100
GSDMD (*cleaved*)	IF	Rabbit mAb IgG	Cell Signaling	(Asp275) #36425	IF: 1/50
GSDME (*total*)	WB	IgG2A	Abnova	Clone 1E10 #H00001687-M01	WB: 1/1000
Caspase-1 (*total*)	WB	Mouse IgG2A	R&D Systems	Clone 661228 #MAB6215	WB: 1/5000
NLRP3	WB	Mouse IgG1	Novus Bio	CLO210, #NBP2-52879	WB: 1/500
Perforin	IF	Mouse IgG2B	BD	#556434	IF: 1/200
Beta-actin	WB	Mouse IgG2A	Sigma Aldrich	Clone AC-74 #A5316	1/5000

1025

1026 **Secondary Antibodies**

Name	Application	Supplier	Identifier	Concentration
Goat anti-Rabbit HRP	WB	Cell Signaling`	7074S	1/2500
Goat anti-Mouse IgG HRP	WB	Cell Signaling	7076S	1/2500
Goat anti-rabbit Alexa Fluor™ Plus 488	IF	Invitrogen	A32731	1/100
Goat anti-Mouse IgG2b Alexa Fluor™ 555	IF	Invitrogen	A21147	1/100
Goat anti-Mouse IgG1 Alexa Fluor™ 647	IF	Invitrogen	A21240	1/100

1027

1028

1029

1030 **Immunofluorescence**

1031 JY target cells were either non-pulsed or pulsed with 10μM antigenic peptide (CMV p65) for 2hr
1032 at 37 °C and 5% CO_2 in RPMI 5% FCS/HEPES, washed three times, and conjugated at an
1033 effector:target ratio of 1:1 with antigen-specific human CTLs using 1 min centrifugation at 455g.
1034 Conjugates were incubated for 5 or 15 min, gently disrupted, and subsequently seeded on Poly-L-
1035 Lysine-coated slides. Cells were fixed with 3% paraformaldehyde at 37 °C for 10min. Cells were
1036 then permeabilized with 0.1% saponin (in PBS/3%BSA/HEPES), and stained with the indicated
1037 primary antibodies overnight at RT followed by isotype-matched secondary antibodies for 1hr at
1038 RT. Samples were washed, mounted in 90% glycerol-PBS containing 2.5% DABCO (Sigma) and
1039 examined using a LSM 880 (Zeiss) confocal microscope using a 63x objective. 3D images (using
1040 the z-stack function) were acquired at 1μm intervals.

1041 To assess GSDMD expression in target cells, cells were manually outlined and the MFI of total
1042 and cleaved GSDMD within the target cell measured (using the Measure function of ImageJ) on 5
1043 different planes of the *z*-stack (separated by 1μm) at the height of the IS and subsequently averaged.
1044 To ensure consistency in the quantification, only target cells in the pre-bubbling stage were
1045 included in the analysis, and cells with highly irregular bubbling protrusions or ruptured
1046 membranes were excluded.

1047 To assess whether total and cleaved GSDMD were expressed evenly throughout the target cell or
1048 enriched proximal to the synapse, each target cell was divided into two halves in the x-y plane
1049 (synaptic and distal) and MFI quantified separately for each half of the cell. This analysis was
1050 repeated in both the cleaved and total GSDMD channels across 5 sequential planes of the z-stack
1051 at the height of the IS and the average ratio of synaptic:distal signal was calculated for each cell.
1052 According to this analysis, a synaptic:distal ratio greater than 1 indicates synaptic enrichment;

1053 equal to 1 indicates even distribution of signal throughout the cell, and less than 1 indicates distal
1054 enrichment. For this analysis, the mean synaptic:distal ratio for each channel was compared to a
1055 hypothetical value of 1 (indicating even intracellular distribution) using a one-sample *t*-test.

1056

1057 **Time Lapse Microscopy**

1058 For drug treatment experiments, JY cells were preloaded with CellMask™ Deep Red plasma
1059 membrane stain (1µg/mL) (Invitrogen, #C10046) for 30 min at 37°C with 5% CO_2, washed, and
1060 then seeded in RPMI 1640 medium with 10% FCS at 2 x 10^5 - 3 x 10^5 cells per well on poly-D-
1061 lysine coated 8-well chambered slides (Ibidi) for 5 min before imaging. Propidium iodide was
1062 added at a concentration of 6.6µg/mL. Drugs were added at the indicated concentrations: nigericin
1063 (100µM), staurosporine (6.7 µM), or solvent control. Timelaspe micrsocopy was performed within
1064 a temperature-controlled chamber using multi position acquisition (3 positions) overnight on a
1065 spinning-disk microscope. All time-lapse microscope experiments were acquired on a spinning
1066 disk microscope equipped with APO lbda 60X NA 1.4 objective. The temperature controlled
1067 chamber was maintained at 37°C and a constant 5% CO2 concentration. A Prime 95B Scientific
1068 sCMOS Camera (Photometrics) was used for acquisition. Image acquisition was controlled by
1069 MetaMorph Software (Molecular Devices 7.10.5.476) and by Modular V2.0 GATACA software.

1070 To analyze the morphological features (cross-sectional area and aspect ratio) of dying target cells
1071 over the duration of the imaging period, target cell masks were generated using ImageJ software
1072 (version 1.53o), using the following semi-automated image processing pipeline: first, images were
1073 split into channels. Then, the variance filter was applied to the transmission channel (radius 5.0)
1074 followed by "Threshold" and "Transform to Binary". Next, the "Erode" binary function option
1075 was applied and manually cross-checked against the transmission channel. Finally, the "Fill Holes"

1076 function was applied and where possible, the "Add Mask" function was utilized to generate the
1077 outline. The "Watershed" function was applied as the final step and manual correction was
1078 performed as needed on a slice-by-slice basis to remove debris and artifacts. "Analyze Particle"
1079 was utilized to draw outlines after manual correction, after which a macro was used to generate the
1080 black background and white foreground, and to label and save the mask area. Thus, a cell mask
1081 was generated for each cell at every time-point throughout the imaging period, from which the
1082 cross-sectional area and aspect ratio could be calculated and plotted over time.

1083 To visualize the morphological features of JY cells dying upon CTL attack, JY cells were pulsed
1084 with 10µM peptide, preloaded with Cell Mask DeepRed plasma membrane stain (1µg/mL)
1085 (Invitrogen), washed and seeded at 2.5 x 10^4 cells per wells on poly-D-lysine coated 16 wells-
1086 chambered slides (Ibidi). CTL clones were preloaded with Fluo-8-AM (0.25ng/µL) (AAT
1087 Bioquest) and SPY650 Tubulin (2X) (Spirochrome) or Tubulin Tracker Deep Red (2.56µg/µL)
1088 (Invitrogen) for 30min, washed and added at 4 x 10^4 to 5 x 10^5 cells per wells. Propidium iodide
1089 (6.6µg/mL) was added immediately before the acquisition. In these experiments, cells were kept
1090 in RPMI 1640 with 5% FCS medium for the imaging period.

1091 For the analysis, the three channels were split (transmission, CellMask, Fluo-8-AM). Then, the
1092 variance filter was applied to the transmission channel (radius 5.0) and a binary option applied
1093 (manually cross-checked against the transmission image). In order to remove the CTL from
1094 analysis, the "Create Mask" function was applied to the Fluo-8-AM channel and subtracted from
1095 the selection (either the Brightfield/variance or CellMask Channel) using Image Calculator.
1096 Finally, the "Fill Holes" and "Watershed" functions were applied and adjusted manually as
1097 required. "Analyze Particle" was utilized as a final step described above.

1098

1099 **Exposure of Targets to Purified SMAPs**

1100 10, 000 JY cells/well were treated for 4 hours with exogenous SMAPs purified from NK-92 cell
1101 supernatant as described (https://doi.org/10.1101/2025.11.10.687675). Briefly, particles were
1102 concentrated using100 kDa Amicon spin filters, soluble proteins were removed using Captocore
1103 columns, SMAPs were purified by S1000 size exclusion chromatography
1104 (https://doi.org/10.1101/2025.11.10.687675). After 4hr, killing modality was assessed using an
1105 Annexin V/PI assay (BD Pharmingen FITC Annexin V Apoptosis Detection Kit I, #AB_2869082)
1106 as described above. Samples were acquired using the MACSQuant Analyzer 10 flow cytometer
1107 (Miltenyi Biotec) and analyzed using FlowJo 10.

1108 **Material Availability**

1109 Materials are available from the authors upon request, subject to the appropriate Material Transfer
1110 Agreements and constrained by the relevant ethical guidelines. All commercial reagents and
1111 materials are available from the indicated sources.

1112 **Statistical Analysis**

1113 Statistical analyses were performed using GraphPad Prism 10.1.2. All tests were 2-sided unless
1114 otherwise indicated. Data distributions were assumed to follow a normal distribution unless
1115 otherwise indicated. Multiple comparisons were performed when more than two groups were being
1116 compared, and the specific tests utilized for multiple comparisons have been indicated throughout
1117 the manuscript.

1118 **REFERENCES**

1119 1 Cassioli, C. & Baldari, C. T. The Expanding Arsenal of Cytotoxic T Cells. *Front Immunol* **13**, 883010,
1120 doi:10.3389/fimmu.2022.883010 (2022).
1121 2 McKenzie, B. & Valitutti, S. Resisting T cell attack: tumor-cell-intrinsic defense and reparation
1122 mechanisms. *Trends Cancer* **9**, 198-211, doi:10.1016/j.trecan.2022.12.003 (2023).
1123 3 McKenzie, B., Khazen, R. & Valitutti, S. Greek Fire, Poison Arrows, and Scorpion Bombs: How
1124 Tumor Cells Defend Against the Siege Weapons of Cytotoxic T Lymphocytes. *Front Immunol* **13**,
1125 894306, doi:10.3389/fimmu.2022.894306 (2022).
1126 4 Balint, S. *et al.* Supramolecular attack particles are autonomous killing entities released from
1127 cytotoxic T cells. *Science* **368**, 897-901, doi:10.1126/science.aay9207 (2020).
1128 5 Jainarayanan, A. *et al.* Isolation of functional supramolecular attack particles (SMAPs). *bioRxiv*,
1129 2025.2011.2010.687675, doi:10.1101/2025.11.10.687675 (2025).
1130 6 Lopez, J. A. *et al.* Perforin forms transient pores on the target cell plasma membrane to facilitate
1131 rapid access of granzymes during killer cell attack. *Blood* **121**, 2659-2668, doi:10.1182/blood-
1132 2012-07-446146 (2013).
1133 7 Filali, L. *et al.* Ultrarapid lytic granule release from CTLs activates Ca(2+)-dependent synaptic
1134 resistance pathways in melanoma cells. *Sci Adv* **8**, eabk3234, doi:10.1126/sciadv.abk3234 (2022).
1135 8 Khazen, R. *et al.* Melanoma cell lysosome secretory burst neutralizes the CTL-mediated
1136 cytotoxicity at the lytic synapse. *Nat Commun* **7**, 10823, doi:10.1038/ncomms10823 (2016).
1137 9 Ritter, A. T. *et al.* ESCRT-mediated membrane repair protects tumor-derived cells against T cell
1138 attack. *Science* **376**, 377-382, doi:10.1126/science.abl3855 (2022).
1139 10 Keefe, D. *et al.* Perforin triggers a plasma membrane-repair response that facilitates CTL
1140 induction of apoptosis. *Immunity* **23**, 249-262, doi:10.1016/j.immuni.2005.08.001 (2005).
1141 11 Weigelin, B. & Friedl, P. T cell-mediated additive cytotoxicity - death by multiple bullets. *Trends*
1142 *Cancer* **8**, 980-987, doi:10.1016/j.trecan.2022.07.007 (2022).
1143 12 Weigelin, B. *et al.* Cytotoxic T cells are able to efficiently eliminate cancer cells by additive
1144 cytotoxicity. *Nat Commun* **12**, 5217, doi:10.1038/s41467-021-25282-3 (2021).
1145 13 Voskoboinik, I., Whisstock, J. C. & Trapani, J. A. Perforin and granzymes: function, dysfunction
1146 and human pathology. *Nat Rev Immunol* **15**, 388-400, doi:10.1038/nri3839 (2015).
1147 14 Ivanova, M. E. *et al.* The pore conformation of lymphocyte perforin. *Sci Adv* **8**, eabk3147,
1148 doi:10.1126/sciadv.abk3147 (2022).
1149 15 Stewart, S. E. *et al.* The perforin pore facilitates the delivery of cationic cargos. *J Biol Chem* **289**,
1150 9172-9181, doi:10.1074/jbc.M113.544890 (2014).
1151 16 Shewell, L. K. *et al.* All major cholesterol-dependent cytolysins use glycans as cellular receptors.
1152 *Sci Adv* **6**, eaaz4926, doi:10.1126/sciadv.aaz4926 (2020).
1153 17 Shinkai, Y., Takio, K. & Okumura, K. Homology of perforin to the ninth component of
1154 complement (C9). *Nature* **334**, 525-527, doi:10.1038/334525a0 (1988).
1155 18 Dal Peraro, M. & van der Goot, F. G. Pore-forming toxins: ancient, but never really out of fashion.
1156 *Nat Rev Microbiol* **14**, 77-92, doi:10.1038/nrmicro.2015.3 (2016).
1157 19 Margheritis, E., Kappelhoff, S. & Cosentino, K. Pore-Forming Proteins: From Pore Assembly to
1158 Structure by Quantitative Single-Molecule Imaging. *Int J Mol Sci* **24**, doi:10.3390/ijms24054528
1159 (2023).
1160 20 Tapia-Abellan, A. *et al.* Sensing low intracellular potassium by NLRP3 results in a stable open
1161 structure that promotes inflammasome activation. *Sci Adv* **7**, eabf4468,
1162 doi:10.1126/sciadv.abf4468 (2021).

1163 21 Swanson, K. V., Deng, M. & Ting, J. P. The NLRP3 inflammasome: molecular activation and
1164 regulation to therapeutics. *Nat Rev Immunol* **19**, 477-489, doi:10.1038/s41577-019-0165-0
1165 (2019).
1166 22 Munoz-Planillo, R. *et al.* K(+) efflux is the common trigger of NLRP3 inflammasome activation by
1167 bacterial toxins and particulate matter. *Immunity* **38**, 1142-1153,
1168 doi:10.1016/j.immuni.2013.05.016 (2013).
1169 23 Gurcel, L., Abrami, L., Girardin, S., Tschopp, J. & van der Goot, F. G. Caspase-1 activation of lipid
1170 metabolic pathways in response to bacterial pore-forming toxins promotes cell survival. *Cell* **126**,
1171 1135-1145, doi:10.1016/j.cell.2006.07.033 (2006).
1172 24 Higa, N. *et al.* Vibrio parahaemolyticus effector proteins suppress inflammasome activation by
1173 interfering with host autophagy signaling. *PLoS Pathog* **9**, e1003142,
1174 doi:10.1371/journal.ppat.1003142 (2013).
1175 25 Craven, R. R. *et al.* Staphylococcus aureus alpha-hemolysin activates the NLRP3-inflammasome in
1176 human and mouse monocytic cells. *PLoS One* **4**, e7446, doi:10.1371/journal.pone.0007446
1177 (2009).
1178 26 Holzinger, D. *et al.* Staphylococcus aureus Panton-Valentine leukocidin induces an inflammatory
1179 response in human phagocytes via the NLRP3 inflammasome. *J Leukoc Biol* **92**, 1069-1081,
1180 doi:10.1189/jlb.0112014 (2012).
1181 27 Liang, H., Wang, B., Wang, J., Ma, B. & Zhang, W. Pyolysin of Trueperella pyogenes Induces
1182 Pyroptosis and IL-1beta Release in Murine Macrophages Through Potassium/NLRP3/Caspase-
1183 1/Gasdermin D Pathway. *Front Immunol* **13**, 832458, doi:10.3389/fimmu.2022.832458 (2022).
1184 28 De Schutter, E. *et al.* Punching Holes in Cellular Membranes: Biology and Evolution of
1185 Gasdermins. *Trends Cell Biol* **31**, 500-513, doi:10.1016/j.tcb.2021.03.004 (2021).
1186 29 Wang, Y. *et al.* Chemotherapy drugs induce pyroptosis through caspase-3 cleavage of a
1187 gasdermin. *Nature* **547**, 99-103, doi:10.1038/nature22393 (2017).
1188 30 Kayagaki, N. *et al.* Caspase-11 cleaves gasdermin D for non-canonical inflammasome signalling.
1189 *Nature* **526**, 666-671, doi:10.1038/nature15541 (2015).
1190 31 Liu, X. *et al.* Inflammasome-activated gasdermin D causes pyroptosis by forming membrane
1191 pores. *Nature* **535**, 153-158, doi:10.1038/nature18629 (2016).
1192 32 Mulvihill, E. *et al.* Mechanism of membrane pore formation by human gasdermin-D. *EMBO J* **37**,
1193 doi:10.15252/embj.201798321 (2018).
1194 33 Ding, J. *et al.* Pore-forming activity and structural autoinhibition of the gasdermin family. *Nature*
1195 **535**, 111-116, doi:10.1038/nature18590 (2016).
1196 34 DiPeso, L., Ji, D. X., Vance, R. E. & Price, J. V. Cell death and cell lysis are separable events during
1197 pyroptosis. *Cell Death Discov* **3**, 17070, doi:10.1038/cddiscovery.2017.70 (2017).
1198 35 Devant, P. & Kagan, J. C. Molecular mechanisms of gasdermin D pore-forming activity. *Nat*
1199 *Immunol* **24**, 1064-1075, doi:10.1038/s41590-023-01526-w (2023).
1200 36 Xia, S. *et al.* Gasdermin D pore structure reveals preferential release of mature interleukin-1.
1201 *Nature* **593**, 607-611, doi:10.1038/s41586-021-03478-3 (2021).
1202 37 Yu, P. *et al.* Pyroptosis: mechanisms and diseases. *Signal Transduct Target Ther* **6**, 128,
1203 doi:10.1038/s41392-021-00507-5 (2021).
1204 38 Ruhl, S. & Broz, P. Regulation of Lytic and Non-Lytic Functions of Gasdermin Pores. *J Mol Biol*
1205 **434**, 167246, doi:10.1016/j.jmb.2021.167246 (2022).
1206 39 Li, Z. *et al.* Enhancing Gasdermin-induced tumor pyroptosis through preventing ESCRT-
1207 dependent cell membrane repair augments antitumor immune response. *Nat Commun* **13**, 6321,
1208 doi:10.1038/s41467-022-34036-8 (2022).
1209 40 Ruhl, S. *et al.* ESCRT-dependent membrane repair negatively regulates pyroptosis downstream of
1210 GSDMD activation. *Science* **362**, 956-960, doi:10.1126/science.aar7607 (2018).

1211 41 Nozaki, K. *et al.* Caspase-7 activates ASM to repair gasdermin and perforin pores. *Nature* **606**,
1212 960-967, doi:10.1038/s41586-022-04825-8 (2022).
1213 42 Shkarina, K. *et al.* Optogenetic activators of apoptosis, necroptosis, and pyroptosis. *J Cell Biol*
1214 **221**, doi:10.1083/jcb.202109038 (2022).
1215 43 Kovacs, S. B. & Miao, E. A. Gasdermins: Effectors of Pyroptosis. *Trends Cell Biol* **27**, 673-684,
1216 doi:10.1016/j.tcb.2017.05.005 (2017).
1217 44 Costigan, A., Hollville, E. & Martin, S. J. Discriminating Between Apoptosis, Necrosis, Necroptosis,
1218 and Ferroptosis by Microscopy and Flow Cytometry. *Curr Protoc* **3**, e951, doi:10.1002/cpz1.951
1219 (2023).
1220 45 Zhang, Y., Chen, X., Gueydan, C. & Han, J. Plasma membrane changes during programmed cell
1221 deaths. *Cell Res* **28**, 9-21, doi:10.1038/cr.2017.133 (2018).
1222 46 Chen, X. *et al.* Pyroptosis is driven by non-selective gasdermin-D pore and its morphology is
1223 different from MLKL channel-mediated necroptosis. *Cell Res* **26**, 1007-1020,
1224 doi:10.1038/cr.2016.100 (2016).
1225 47 Liu, X., Xia, S., Zhang, Z., Wu, H. & Lieberman, J. Channelling inflammation: gasdermins in
1226 physiology and disease. *Nat Rev Drug Discov* **20**, 384-405, doi:10.1038/s41573-021-00154-z
1227 (2021).
1228 48 Zychlinsky, A., Zheng, L. M., Liu, C. C. & Young, J. D. Cytolytic lymphocytes induce both apoptosis
1229 and necrosis in target cells. *J Immunol* **146**, 393-400 (1991).
1230 49 Blanchard, D. K. *et al.* Role of extracellular adenosine triphosphate in the cytotoxic T-
1231 lymphocyte-mediated lysis of antigen presenting cells. *Blood* **85**, 3173-3182 (1995).
1232 50 Waterhouse, N. J. *et al.* Cytotoxic T lymphocyte-induced killing in the absence of granzymes A
1233 and B is unique and distinct from both apoptosis and perforin-dependent lysis. *J Cell Biol* **173**,
1234 133-144, doi:10.1083/jcb.200510072 (2006).
1235 51 Jaime-Sanchez, P. *et al.* Cell death induced by cytotoxic CD8(+) T cells is immunogenic and primes
1236 caspase-3-dependent spread immunity against endogenous tumor antigens. *J Immunother*
1237 *Cancer* **8**, doi:10.1136/jitc-2020-000528 (2020).
1238 52 Martinez-Lostao, L., Anel, A. & Pardo, J. How Do Cytotoxic Lymphocytes Kill Cancer Cells? *Clin*
1239 *Cancer Res* **21**, 5047-5056, doi:10.1158/1078-0432.CCR-15-0685 (2015).
1240 53 Zhou, Z. *et al.* Granzyme A from cytotoxic lymphocytes cleaves GSDMB to trigger pyroptosis in
1241 target cells. *Science* **368**, doi:10.1126/science.aaz7548 (2020).
1242 54 Zhang, Z. *et al.* Gasdermin E suppresses tumour growth by activating anti-tumour immunity.
1243 *Nature* **579**, 415-420, doi:10.1038/s41586-020-2071-9 (2020).
1244 55 Liu, Y. *et al.* Gasdermin E-mediated target cell pyroptosis by CAR T cells triggers cytokine release
1245 syndrome. *Sci Immunol* **5**, doi:10.1126/sciimmunol.aax7969 (2020).
1246 56 Galluzzi, L. *et al.* Molecular mechanisms of cell death: recommendations of the Nomenclature
1247 Committee on Cell Death 2018. *Cell Death Differ* **25**, 486-541, doi:10.1038/s41418-017-0012-4
1248 (2018).
1249 57 Reiss, C. S. *et al.* Development and characterization of allospecific long-term human cytolytic T-
1250 cell lines. *Proc Natl Acad Sci U S A* **77**, 5432-5436, doi:10.1073/pnas.77.9.5432 (1980).
1251 58 Caramalho, I., Faroudi, M., Padovan, E., Muller, S. & Valitutti, S. Visualizing CTL/melanoma cell
1252 interactions: multiple hits must be delivered for tumour cell annihilation. *J Cell Mol Med* **13**,
1253 3834-3846, doi:10.1111/j.1582-4934.2008.00586.x (2009).
1254 59 Faroudi, M. *et al.* Lytic versus stimulatory synapse in cytotoxic T lymphocyte/target cell
1255 interaction: manifestation of a dual activation threshold. *Proc Natl Acad Sci U S A* **100**, 14145-
1256 14150, doi:10.1073/pnas.2334336100 (2003).
1257 60 Nagahama, M. *et al.* The p38 MAPK and JNK pathways protect host cells against Clostridium
1258 perfringens beta-toxin. *Infect Immun* **81**, 3703-3708, doi:10.1128/IAI.00579-13 (2013).

1259 61 Rana, P. S. *et al.* Calibration and characterization of intracellular Asante Potassium Green probes,
1260 APG-2 and APG-4. *Anal Biochem* **567**, 8-13, doi:10.1016/j.ab.2018.11.024 (2019).
1261 62 Wong, F. *et al.* Cytoplasmic condensation induced by membrane damage is associated with
1262 antibiotic lethality. *Nat Commun* **12**, 2321, doi:10.1038/s41467-021-22485-6 (2021).
1263 63 Camilli, G. *et al.* beta-Glucan-induced reprogramming of human macrophages inhibits NLRP3
1264 inflammasome activation in cryopyrinopathies. *J Clin Invest* **130**, 4561-4573,
1265 doi:10.1172/JCI134778 (2020).
1266 64 Ren, G. *et al.* ABRO1 promotes NLRP3 inflammasome activation through regulation of NLRP3
1267 deubiquitination. *EMBO J* **38**, doi:10.15252/embj.2018100376 (2019).
1268 65 Perregaux, D. & Gabel, C. A. Interleukin-1 beta maturation and release in response to ATP and
1269 nigericin. Evidence that potassium depletion mediated by these agents is a necessary and
1270 common feature of their activity. *J Biol Chem* **269**, 15195-15203 (1994).
1271 66 Walev, I., Reske, K., Palmer, M., Valeva, A. & Bhakdi, S. Potassium-inhibited processing of IL-1
1272 beta in human monocytes. *EMBO J* **14**, 1607-1614, doi:10.1002/j.1460-2075.1995.tb07149.x
1273 (1995).
1274 67 Russo, H. M. *et al.* Active Caspase-1 Induces Plasma Membrane Pores That Precede Pyroptotic
1275 Lysis and Are Blocked by Lanthanides. *J Immunol* **197**, 1353-1367,
1276 doi:10.4049/jimmunol.1600699 (2016).
1277 68 Rozario, P. *et al.* Mechanistic basis for potassium efflux-driven activation of the human NLRP1
1278 inflammasome. *Proc Natl Acad Sci U S A* **121**, e2309579121, doi:10.1073/pnas.2309579121
1279 (2024).
1280 69 Sun, Y. & Guo, Y. Expression of Caspase-1 in breast cancer tissues and its effects on cell
1281 proliferation, apoptosis and invasion. *Oncol Lett* **15**, 6431-6435, doi:10.3892/ol.2018.8176
1282 (2018).
1283 70 Zheng, W. *et al.* Caspase-1-dependent spatiality in triple-negative breast cancer and response to
1284 immunotherapy. *Nat Commun* **15**, 8514, doi:10.1038/s41467-024-52553-6 (2024).
1285 71 Duhalde Vega, M. *et al.* PD-1/PD-L1 blockade abrogates a dysfunctional innate-adaptive immune
1286 axis in critical beta-coronavirus disease. *Sci Adv* **8**, eabn6545, doi:10.1126/sciadv.abn6545
1287 (2022).
1288 72 Clark, K. M. *et al.* Chemical inhibition of DPP9 sensitizes the CARD8 inflammasome in HIV-1-
1289 infected cells. *Nat Chem Biol* **19**, 431-439, doi:10.1038/s41589-022-01182-5 (2023).
1290 73 Yu, J. *et al.* Inflammasome activation leads to Caspase-1-dependent mitochondrial damage and
1291 block of mitophagy. *Proc Natl Acad Sci U S A* **111**, 15514-15519, doi:10.1073/pnas.1414859111
1292 (2014).
1293 74 Boucher, D. *et al.* Caspase-1 self-cleavage is an intrinsic mechanism to terminate inflammasome
1294 activity. *J Exp Med* **215**, 827-840, doi:10.1084/jem.20172222 (2018).
1295 75 Mitchell, P. S., Sandstrom, A. & Vance, R. E. The NLRP1 inflammasome: new mechanistic insights
1296 and unresolved mysteries. *Curr Opin Immunol* **60**, 37-45, doi:10.1016/j.coi.2019.04.015 (2019).
1297 76 Yang, X. *et al.* Granzyme B mimics apical caspases. Description of a unified pathway for trans-
1298 activation of executioner caspase-3 and -7. *J Biol Chem* **273**, 34278-34283,
1299 doi:10.1074/jbc.273.51.34278 (1998).
1300 77 Adrain, C., Murphy, B. M. & Martin, S. J. Molecular ordering of the caspase activation cascade
1301 initiated by the cytotoxic T lymphocyte/natural killer (CTL/NK) protease granzyme B. *J Biol Chem*
1302 **280**, 4663-4673, doi:10.1074/jbc.M410915200 (2005).
1303 78 Nakazato, K. & Hatano, Y. Monensin-mediated antiport of Na+ and H+ across liposome
1304 membrane. *Biochim Biophys Acta* **1064**, 103-110, doi:10.1016/0005-2736(91)90416-6 (1991).

1305 79 Kataoka, T. *et al.* Concanamycin A, a powerful tool for characterization and estimation of
1306 contribution of perforin- and Fas-based lytic pathways in cell-mediated cytotoxicity. *J Immunol*
1307 **156**, 3678-3686 (1996).
1308 80 Miao, R. *et al.* Gasdermin D permeabilization of mitochondrial inner and outer membranes
1309 accelerates and enhances pyroptosis. *Immunity* **56**, 2523-2541 e2528,
1310 doi:10.1016/j.immuni.2023.10.004 (2023).
1311 81 Khazen, R., Muller, S., Lafouresse, F., Valitutti, S. & Cussat-Blanc, S. Sequential adjustment of
1312 cytotoxic T lymphocyte densities improves efficacy in controlling tumor growth. *Sci Rep* **9**, 12308,
1313 doi:10.1038/s41598-019-48711-2 (2019).
1314 82 Yan, H. *et al.* Cisplatin Induces Pyroptosis via Activation of MEG3/NLRP3/caspase-1/GSDMD
1315 Pathway in Triple-Negative Breast Cancer. *Int J Biol Sci* **17**, 2606-2621, doi:10.7150/ijbs.60292
1316 (2021).
1317 83 Zhang, Z. *et al.* Caspase-3-mediated GSDME induced Pyroptosis in breast cancer cells through the
1318 ROS/JNK signalling pathway. *J Cell Mol Med* **25**, 8159-8168, doi:10.1111/jcmm.16574 (2021).
1319 84 McKenzie, B. A. *et al.* Activation of the executioner caspases-3 and -7 promotes microglial
1320 pyroptosis in models of multiple sclerosis. *J Neuroinflammation* **17**, 253, doi:10.1186/s12974-
1321 020-01902-5 (2020).
1322 85 McKenzie, B. A. *et al.* Caspase-1 inhibition prevents glial inflammasome activation and pyroptosis
1323 in models of multiple sclerosis. *Proc Natl Acad Sci U S A* **115**, E6065-E6074,
1324 doi:10.1073/pnas.1722041115 (2018).
1325 86 Megli, C., Morosky, S., Rajasundaram, D. & Coyne, C. B. Inflammasome signaling in human
1326 placental trophoblasts regulates immune defense against Listeria monocytogenes infection. *J Exp*
1327 *Med* **218**, doi:10.1084/jem.20200649 (2021).
1328 87 Ma, H., Jeppesen, J. F. & Jaenisch, R. Human T Cells Expressing a CD19 CAR-T Receptor Provide
1329 Insights into Mechanisms of Human CD19-Positive beta Cell Destruction. *Cell Rep Med* **1**, 100097,
1330 doi:10.1016/j.xcrm.2020.100097 (2020).
1331 88 Mariathasan, S. *et al.* Cryopyrin activates the inflammasome in response to toxins and ATP.
1332 *Nature* **440**, 228-232, doi:10.1038/nature04515 (2006).
1333 89 Flores, J. *et al.* Caspase-1 inhibition alleviates cognitive impairment and neuropathology in an
1334 Alzheimer's disease mouse model. *Nat Commun* **9**, 3916, doi:10.1038/s41467-018-06449-x
1335 (2018).
1336 90 Dhani, S., Zhao, Y. & Zhivotovsky, B. A long way to go: caspase inhibitors in clinical use. *Cell Death*
1337 *Dis* **12**, 949, doi:10.1038/s41419-021-04240-3 (2021).
1338 91 Hassin, D., Garber, O. G., Meiraz, A., Schiffenbauer, Y. S. & Berke, G. Cytotoxic T lymphocyte
1339 perforin and Fas ligand working in concert even when Fas ligand lytic action is still not
1340 detectable. *Immunology* **133**, 190-196, doi:10.1111/j.1365-2567.2011.03426.x (2011).
1341 92 Meiraz, A., Garber, O. G., Harari, S., Hassin, D. & Berke, G. Switch from perforin-expressing to
1342 perforin-deficient CD8(+) T cells accounts for two distinct types of effector cytotoxic T
1343 lymphocytes in vivo. *Immunology* **128**, 69-82, doi:10.1111/j.1365-2567.2009.03072.x (2009).
1344 93 Prager, I. *et al.* NK cells switch from granzyme B to death receptor-mediated cytotoxicity during
1345 serial killing. *J Exp Med* **216**, 2113-2127, doi:10.1084/jem.20181454 (2019).
1346 94 Chang, H. F. *et al.* Identification of distinct cytotoxic granules as the origin of supramolecular
1347 attack particles in T lymphocytes. *Nat Commun* **13**, 1029, doi:10.1038/s41467-022-28596-y
1348 (2022).
1349 95 Ambrose, A. R., Hazime, K. S., Worboys, J. D., Niembro-Vivanco, O. & Davis, D. M. Synaptic
1350 secretion from human natural killer cells is diverse and includes supramolecular attack particles.
1351 *Proc Natl Acad Sci U S A* **117**, 23717-23720, doi:10.1073/pnas.2010274117 (2020).

1352 96 Kimman, T. *et al.* Serpin B9 controls tumor cell killing by CAR T cells. *J Immunother Cancer* **11**,
1353 doi:10.1136/jitc-2022-006364 (2023).
1354 97 Jiang, P. *et al.* Signatures of T cell dysfunction and exclusion predict cancer immunotherapy
1355 response. *Nat Med* **24**, 1550-1558, doi:10.1038/s41591-018-0136-1 (2018).
1356 98 Gonzalez, M. R. *et al.* Pore-forming toxins induce multiple cellular responses promoting survival.
1357 *Cell Microbiol* **13**, 1026-1043, doi:10.1111/j.1462-5822.2011.01600.x (2011).
1358 99 Demeersseman, L. *et al.* Stenocytosis: a mechanism for supramolecular attack particle transfer at
1359 the CTL lytic synapse. *bioRxiv*, 2025.2011.2005.686769, doi:10.1101/2025.11.05.686769 (2025).
1360 100 Gong, T., Yang, Y., Jin, T., Jiang, W. & Zhou, R. Orchestration of NLRP3 Inflammasome Activation
1361 by Ion Fluxes. *Trends Immunol* **39**, 393-406, doi:10.1016/j.it.2018.01.009 (2018).
1362 101 Barnett, K. C., Li, S., Liang, K. & Ting, J. P. A 360 degrees view of the inflammasome: Mechanisms
1363 of activation, cell death, and diseases. *Cell* **186**, 2288-2312, doi:10.1016/j.cell.2023.04.025
1364 (2023).
1365 102 Yao, Y. *et al.* Antigen-specific CD8(+) T cell feedback activates NLRP3 inflammasome in antigen-
1366 presenting cells through perforin. *Nat Commun* **8**, 15402, doi:10.1038/ncomms15402 (2017).
1367 103 Agard, N. J., Maltby, D. & Wells, J. A. Inflammatory stimuli regulate caspase substrate profiles.
1368 *Mol Cell Proteomics* **9**, 880-893, doi:10.1074/mcp.M900528-MCP200 (2010).
1369 104 Shao, W., Yeretssian, G., Doiron, K., Hussain, S. N. & Saleh, M. The caspase-1 digestome identifies
1370 the glycolysis pathway as a target during infection and septic shock. *J Biol Chem* **282**, 36321-
1371 36329, doi:10.1074/jbc.M708182200 (2007).
1372 105 Loveless, R., Bloomquist, R. & Teng, Y. Pyroptosis at the forefront of anticancer immunity. *J Exp*
1373 *Clin Cancer Res* **40**, 264, doi:10.1186/s13046-021-02065-8 (2021).
1374 106 Rogers, C. *et al.* Gasdermin pores permeabilize mitochondria to augment caspase-3 activation
1375 during apoptosis and inflammasome activation. *Nat Commun* **10**, 1689, doi:10.1038/s41467-019-
1376 09397-2 (2019).
1377 107 de Vasconcelos, N. M., Van Opdenbosch, N., Van Gorp, H., Parthoens, E. & Lamkanfi, M. Single-
1378 cell analysis of pyroptosis dynamics reveals conserved GSDMD-mediated subcellular events that
1379 precede plasma membrane rupture. *Cell Death Differ* **26**, 146-161, doi:10.1038/s41418-018-
1380 0106-7 (2019).
1381 108 Vasconcelos, Z. *et al.* Individual Human Cytotoxic T Lymphocytes Exhibit Intraclonal
1382 Heterogeneity during Sustained Killing. *Cell Rep* **11**, 1474-1485, doi:10.1016/j.celrep.2015.05.002
1383 (2015).
1384 109 Lemaitre, F., Moreau, H. D., Vedele, L. & Bousso, P. Phenotypic CD8+ T cell diversification occurs
1385 before, during, and after the first T cell division. *J Immunol* **191**, 1578-1585,
1386 doi:10.4049/jimmunol.1300424 (2013).
1387 110 Kelso, A. *et al.* The genes for perforin, granzymes A-C and IFN-gamma are differentially expressed
1388 in single CD8(+) T cells during primary activation. *Int Immunol* **14**, 605-613,
1389 doi:10.1093/intimm/dxf028 (2002).
1390 111 Cortacero, K. *et al.* Evolutionary design of explainable algorithms for biomedical image
1391 segmentation. *Nat Commun* **14**, 7112, doi:10.1038/s41467-023-42664-x (2023).
1392 112 Ramirez-Labrada, A. *et al.* All About (NK Cell-Mediated) Death in Two Acts and an Unexpected
1393 Encore: Initiation, Execution and Activation of Adaptive Immunity. *Front Immunol* **13**, 896228,
1394 doi:10.3389/fimmu.2022.896228 (2022).
1395 113 Fisher, R., Pusztai, L. & Swanton, C. Cancer heterogeneity: implications for targeted therapeutics.
1396 *Br J Cancer* **108**, 479-485, doi:10.1038/bjc.2012.581 (2013).
1397 114 Hanahan, D. & Weinberg, R. A. The hallmarks of cancer. *Cell* **100**, 57-70, doi:10.1016/s0092-
1398 8674(00)81683-9 (2000).

1399 115 Hanahan, D. & Weinberg, R. A. Hallmarks of cancer: the next generation. *Cell* **144**, 646-674,
1400 doi:10.1016/j.cell.2011.02.013 (2011).
1401 116 Hanahan, D. Hallmarks of Cancer: New Dimensions. *Cancer Discov* **12**, 31-46, doi:10.1158/2159-
1402 8290.CD-21-1059 (2022).
1403 117 Zapatka, M. *et al.* The landscape of viral associations in human cancers. *Nat Genet* **52**, 320-330,
1404 doi:10.1038/s41588-019-0558-9 (2020).
1405 118 Fan, J. X. *et al.* Epigenetics-Based Tumor Cells Pyroptosis for Enhancing the Immunological Effect
1406 of Chemotherapeutic Nanocarriers. *Nano Lett* **19**, 8049-8058, doi:10.1021/acs.nanolett.9b03245
1407 (2019).
1408 119 Erkes, D. A. *et al.* Mutant BRAF and MEK Inhibitors Regulate the Tumor Immune
1409 Microenvironment via Pyroptosis. *Cancer Discov* **10**, 254-269, doi:10.1158/2159-8290.CD-19-
1410 0672 (2020).
1411 120 Lu, H. *et al.* Molecular Targeted Therapies Elicit Concurrent Apoptotic and GSDME-Dependent
1412 Pyroptotic Tumor Cell Death. *Clin Cancer Res* **24**, 6066-6077, doi:10.1158/1078-0432.CCR-18-
1413 1478 (2018).
1414 121 Liu, Y. G. *et al.* NLRP3 inflammasome activation mediates radiation-induced pyroptosis in bone
1415 marrow-derived macrophages. *Cell Death Dis* **8**, e2579, doi:10.1038/cddis.2016.460 (2017).
1416 122 Tan, G. *et al.* Radiosensitivity of colorectal cancer and radiation-induced gut damages are
1417 regulated by gasdermin E. *Cancer Lett* **529**, 1-10, doi:10.1016/j.canlet.2021.12.034 (2022).
1418 123 Li, H. *et al.* Pyroptotic cell death: an emerging therapeutic opportunity for radiotherapy. *Cell*
1419 *Death Discov* **10**, 32, doi:10.1038/s41420-024-01802-0 (2024).
1420 124 Wang, Q. *et al.* A bioorthogonal system reveals antitumour immune function of pyroptosis.
1421 *Nature* **579**, 421-426, doi:10.1038/s41586-020-2079-1 (2020).
1422 125 Zhang, Z., Zhang, Y. & Lieberman, J. Lighting a Fire: Can We Harness Pyroptosis to Ignite
1423 Antitumor Immunity? *Cancer Immunol Res* **9**, 2-7, doi:10.1158/2326-6066.CIR-20-0525 (2021).
1424 126 Phulphagar, K. *et al.* Proteomics reveals distinct mechanisms regulating the release of cytokines
1425 and alarmins during pyroptosis. *Cell Rep* **34**, 108826, doi:10.1016/j.celrep.2021.108826 (2021).
1426 127 Mellman, I., Chen, D. S., Powles, T. & Turley, S. J. The cancer-immunity cycle: Indication,
1427 genotype, and immunotype. *Immunity* **56**, 2188-2205, doi:10.1016/j.immuni.2023.09.011 (2023).
1428 128 Holley, C. L. *et al.* Pyroptotic cell corpses are crowned with F-actin-rich filopodia that engage
1429 CLEC9A signaling in incoming dendritic cells. *Nat Immunol*, doi:10.1038/s41590-024-02024-3
1430 (2024).
1431 129 Deng, T., Tang, C., Zhang, G. & Wan, X. DAMPs released by pyroptotic cells as major contributors
1432 and therapeutic targets for CAR-T-related toxicities. *Cell Death Dis* **12**, 129, doi:10.1038/s41419-
1433 021-03428-x (2021).
1434 130 Luri-Rey, C. *et al.* Cytotoxicity as a form of immunogenic cell death leading to efficient tumor
1435 antigen cross-priming. *Immunol Rev* **321**, 143-151, doi:10.1111/imr.13281 (2024).
1436 131 Li, S. *et al.* Gasdermin D in peripheral myeloid cells drives neuroinflammation in experimental
1437 autoimmune encephalomyelitis. *J Exp Med* **216**, 2562-2581, doi:10.1084/jem.20190377 (2019).
1438 132 McKenzie, B. A., Dixit, V. M. & Power, C. Fiery Cell Death: Pyroptosis in the Central Nervous
1439 System. *Trends Neurosci* **43**, 55-73, doi:10.1016/j.tins.2019.11.005 (2020).
1440 133 Wu, Y. *et al.* Cell pyroptosis in health and inflammatory diseases. *Cell Death Discov* **8**, 191,
1441 doi:10.1038/s41420-022-00998-3 (2022).
1442 134 Welz, M. *et al.* Perforin inhibition protects from lethal endothelial damage during fulminant viral
1443 hepatitis. *Nat Commun* **9**, 4805, doi:10.1038/s41467-018-07213-x (2018).

1444

Acknowledgements

We thank the members of the European Research Council ATTACK consortium for their discussion and Dr. Eric Espinosa and Dr. Cosima Baldari for their helpful critiques of this manuscript. We thank the flow cytometry and microscopy core facilities of the INSERM UMR 1037 (CRCT). Parts of the figures (e.g. organelles, membranes) were drawn by using pictures from Servier Medical Art, which is licensed under a Creative Commons Attribution 3.0 Unported License. This research in this manuscript has received funding from the European Research Council (**ERC**) under the European Union's Horizon 2020 Research and Innovation Programme (Grant agreement No. Syn- 951329). The research was also supported by INSERM institutional funding, from the Fondation Toulouse Cancer Santé and from the Oncopole Claudius-Regaud. Funders had no role in the preparation of this manuscript.

Author contributions

BM designed the research, performed experiments, analyzed results, and wrote the paper. MPP, FR, LD, EC, AB, and SM performed experiments, analyzed data, and edited the paper. AJ, MW, CS, LC provided reagents, MLD discussed results and provided research insights, SV supervised the research, designed the project, and wrote the paper.

Competing interests

BM is co-founder of Mantalys France SAS. MLD and AJ are co-founder of Granza Bio ldt. SV has a research agreement with Granza Bio. The other authors declare they have no competing interests.

Data Availability

All original data generated for this study will be deposited in figshare repository server (https://figshare.com/) with a unique identifier listed here upon acceptance of this article.

1467

1468 **Figure 1| Potassium efflux from target cells occurs upon CTL attack and exposure to soluble perforin**

1469 **a,b.** JY target cells were pulsed or not with 10µM antigenic peptide, stained with the fluorescent potassium
1470 indicator Ion Potassium Green (**IPG-2 AM**), conjugated with antigen-specific CTLs at the indicated E:T
1471 ratios for 5 or 15 min, and assessed using flow cytometry. Representative histograms are shown, with the
1472 IPG-2 AM^{Bright} population indicated by black bars. **c,d.** Quantification of the percentage of target cells in
1473 the IPG-2 AM^{Bright} gate after 5min (**c.**) and 15min (**d.**) conjugation. Each datapoint represents the average
1474 of two technical replicates from an individual experiment, with n=4 independent experiments represented
1475 on the graph. Two-way ANOVA with Sidak's multiple comparison test was utilized to assess statistical
1476 significance. **e.** JY target cells were preloaded with IPG-2 AM, treated with either solvent control or the
1477 indicated concentrations of recombinant human perforin in calcium-enriched perforin binding buffer for 5
1478 or 15min, and assessed by flow cytometry. Representative histograms are shown, with the IPG-2 AM^{Bright}
1479 population indicated by black bars. **f,g.** Quantification of the percentage of IPG-2 AM^{Bright} target cells after
1480 5min (**f.**) and 15min (**g.**). Each datapoint represents the average of two technical replicates from an
1481 individual experiment, with n=5 independent experiments represented on the graph. Horizontal black lines
1482 represent the mean of independent experiments. One-way ANOVA with Sidak's test for multiple
1483 comparisons was utilized to assess statistical differences. *$p<0.05$, ** $p<0.01$, *** $p<0.001$, ns = not
1484 significant.

1485

1486 **Figure 2| Caspase-1 is activated in JY target cells upon CTL attack and exposure to soluble perforin**

1487 **a-c.** JY target cells were pulsed with 10μM antigenic peptide and conjugated with CTLs at an E:T ratio of
1488 4:1 for 5 or 15 min, before being stained with an activity-dependent fluorescent caspase-1 probe and
1489 assessed by flow cytometry. Non-pulsed target cells were conjugated with CTLs under identical conditions
1490 for 15min as a control. **a.** Representative histograms shown. Black bars represent targets with high caspase-
1491 1 activity. **b.** Quantification of the percentage of target cells in the high caspase-1 activity gate. Each
1492 datapoint represents the average of two technical replicates from an individual experiment, with a total of
1493 n=8 independent experiments represented on the graph. Horizontal black lines represent the mean of
1494 independent experiments for each condition. One-way ANOVA with Dunnet's test for multiple comparisons
1495 was utilized to assess statistical significance. **c.** Median caspase-1 fluorescence intensity from the
1496 experiments shown in (**b.**), represented as fold increase over non-pulsed control (dotted horizontal line).
1497 One-sample *t*-tests were utilized to compare each time point to the hypothetical value of 1.0, representing
1498 the non-pulsed control. **d.** JY cells were pulsed with the indicated concentration of antigenic peptide at an
1499 E:T ratio of 4:1 for 15min and assessed as in **a-c.** Data shown represent mean +/- SEM, n=5 independent
1500 experiments (each with two technical replicates per condition). One-way ANOVA with Dunnet's test for
1501 multiple comparisons was utilized to assess statistical significance. **e.** JY cells were pulsed with 10μM
1502 antigenic peptide and conjugated with CTLs at the indicated E:T ratios for 15min and assessed as above.
1503 Each datapoint represents the average of two technical replicates from an individual experiment, with n=7
1504 independent experiments represented on the graph. Bars represent the mean of independent experiments.
1505 Two-way ANOVA with Sidak's multiple comparison test was utilized to assess statistical significance. **f.**
1506 JY target cells were transfected with non-targeting (**NTsiRNA**) or NLRP3-targeting siRNA (***NLRP3***
1507 **siRNA**) for 24hr before being pulsed or not with 10μM antigenic peptide and conjugated with CTLs at an
1508 E:T ratio of 4:1 for 15 min. JY cells were stained with the fluorescent caspase-1 probe as above. Data shown
1509 represent the fold increase in caspase-1 median fluorescence intensity relative to non-pulsed controls
1510 (indicated by dotted line) for NT siRNA and NLRP3-targeting siRNA respectively (n=6 biological

1511 experiments). A ratio paired *t*-test was utilized to assess statistical differences. **g.** JY cells were pulsed or
1512 not with 10μM antigenic peptide and conjugated for 15min at an E:T ratio of 4:1 with CTLs that had been
1513 pre-treated with either solvent or monensin (to de-acidify lytic granules) before being stained with the
1514 fluorescent caspase-1 probe. Each datapoint represents the average of two technical replicates from an
1515 individual experiment, with n=8 independent experiments represented on the graph. Horizontal black lines
1516 represent the mean of independent experiments for each condition. Ordinary one-way ANOVA with
1517 Tukey's test for multiple comparisons was utilized to assess statistical significance. **h.** JY cells were pre-
1518 loaded with caspase-1 probe in perforin binding buffer, treated with solvent control or 8μg/mL recombinant
1519 human perforin for 30min, and assessed by flow cytometry. Each datapoint represents the average of two
1520 technical replicates from an individual experiment, with n=4 independent experiments represented on the
1521 graph. Bars represent mean +/- SEM. Paired *t*-test was utilized to assess statistical difference. **i.** In parallel,
1522 JY cells were pre-loaded with caspase-1 probe in high-potassium perforin binding buffer, treated with
1523 8μg/mL recombinant human perforin for 30min and assessed by flow cytometry. Each datapoint represents
1524 the average of two technical replicates from an individual experiment, with n=4 independent experiments
1525 represented on the graph. A ratio paired *t*-test was utilized to assess statistical difference.

1526

1527

1528

1529 **Figure 3| Cleaved GSDMD is detectable upon CTL attack and is enriched adjacent to the synapse**

1530 **a-d.** JY target cells were pulsed with 10μM antigenic peptide and conjugated at an E:T ratio of 1:1 with
1531 antigen-specific human CTLs for 15min. Conjugates were fixed and subject to immunostaining for total
1532 GSDMD, cleaved GSDMD and perforin. **a.** 3D reconstruction with total GSDMD (*blue*), cleaved GSDMD
1533 (*green*) and perforin (*red*). **b.** Representative conjugates from non-pulsed and pulsed conditions, with total
1534 and cleaved GSDMD shown in pseudocolor and perforin in red. Images shown are from a single plane of
1535 the *z*-stack and are illustrative examples from n=4 biological experiments. **c.** Schematic for the
1536 quantification of cleaved and total GSDMD mean fluorescence intensity (**MFI**) within the target cell mask
1537 across five sequential planes of the *z*-stack. The five planes were chosen to correspond to the height of the
1538 lytic synapse in the *z*-dimension and MFI averaged across the five planes. **d-e.** MFI of total **(d.)** and cleaved
1539 **(e.)** GSDMD within the target cell mask was measured on 5 sequential planes of the *z*-stack (separated by
1540 1μm) at the height of the lytic synapse and subsequently averaged. Each datapoint corresponds to one target
1541 cell, from n=4 biological experiments. Statistical differences between groups were assessed by unpaired *t*-
1542 tests. **f-i.** Target cells and CTLs were prepared as above and conjugated for 5min before being subjected to
1543 immunostaining and quantification as described above. **g.** Schematic for the quantification of cleaved and
1544 total GSDMD MFI across five sequential planes of the *z*-stack. **h-i.** MFI of total **(h.)** and cleaved **(i.)**
1545 GSDMD within the target cell was measured on 5 different planes of the *z*-stack (separated by 1μm) at the
1546 height of the synpase and subsequently averaged. Each datapoint corresponds to one target cell, from n=4
1547 biological experiments. **j,k.** To assess whether cleaved or total GSDMD was enriched proximal to the
1548 synapse, each target cell mask was divided in half in the *x*-*y* dimension to create "synaptic" and "distal"
1549 masks, for which MFI was separately quantified. The ratio of synaptic:distal signal was calculated and
1550 averaged across the 5 sequential planes. Ratios higher than 1 indicate synaptic enrichment, lower than 1
1551 indicates distal enrichment, and equal to 1 indicates even distribution throughout the cell. Each datapoint
1552 represents the average ratio of synaptic:distal signal across 5 planes for a single cell. Mean ratio of
1553 synaptic:distal MFI for both cleaved and total GSDMD were compared to a hypothetical value of 1

1554 (indicating even distribution of signal throughout the cell) using one-sample *t*-tests. Scale bars are 5μm.

1555 Error bars represent mean +/- SEM. ** $p<0.01$, *** $p<0.01$, **** $p<0.0001$, ns = non-significant.

1556

1557 **Figure 4| Target cells die by pyroptosis upon CTL attack**

1558 **a,b.** JY target cells were pulsed with 10μM antigenic peptide, and conjugated at an E:T ratio of 1:1 with
1559 antigen-specific human CTLs pre-loaded with Fluo-8-AM (*green*) and SPY650 Tubulin (*magenta*) in the
1560 presence of 6.6μg/mL propidium iodide (*red*). Conjugate formation and cell death morphology was assessed
1561 using spinning disk time lapse microscopy for 2hr. Snapshots (from **Supplementary Movie 1** and **2**)
1562 illustrate various stages of CTL attack including initial CTL contact, MTOC polarization (*magenta arrows*),
1563 synapse formation (*black arrows*), pyroptotic body formation (*white arrows*), and loss of membrane
1564 integrity, indicated by PI entry. Two representative examples from n=3 independent experiments are shown;
1565 additional examples are shown in **Supplementary Figure 8**. Scale bar is 10μm. **c,d.** JY cells were pulsed
1566 or non-pulsed (**NP**) with antigenic peptide and conjugated at an E:T ratio of 4:1 with antigen-specific human
1567 CTLs for 1 or 4 hours. Following conjugation, cells were subjected to Annexin V/PI staining and analyzed
1568 by flow cytometry. **c.** Representative dotplots of target cells from n=6 biological experiments. **d**. Data shown
1569 represent the percentage of target cells in each quadrant (Annexin V/PI double positive, Annexin V single-
1570 positive, PI single-positive, or double negative) at the indicated time points. Each datapoint represents the
1571 average of two technical replicates from an individual experiment, with n=6 independent experiments
1572 represented on the graph. Black bars represent the mean of n=6 biological experiments. Repeated
1573 measurement one-way ANOVA with Tukey's test for multiple comparisons was utilized to assess statistical
1574 significance. **e.** Antigen-pulsed or NP JY cells were conjugated at a 4:1 E:T ratio with CTLs for 1hr and
1575 supernatants subjected to luminescent HMGB1 immunoassay. Results shown represent the difference in
1576 luminescence between pulsed and non-pulsed conditions. Datapoints represent the average of two technical
1577 replicates from an individual biological experiment, with a total of n=6 independent experiments represented
1578 on the graph. A paired *t*-test was utilized to assess statistical significance. **f.** Antigen-pulsed or non-pulsed
1579 JY cells were conjugated at a 4:1 E:T ratio with CTLs for 4hr and supernatants subjected to LDH activity
1580 assay. Results shown indicate OD450 values (with background subtracted). Each datapoint represents the
1581 average of two technical replicates from an individual experiment, with n=6 independent experiments

represented on the graph. A paired *t*-test was utilized to assess statistical significance. **g.** JY cells were pulsed or non-pulsed with antigenic peptide and conjugated at an E:T ratio of 4:1 with CTLs that had been pre-treated or not with monensin to de-acidify lytic granules. After 4hr conjugation, cells were subjected to Annexin V/PI staining and analyzed by flow cytometry. Data shown represent the percentage of target cells in the Annexin V/PI double-positive quadrant. Each datapoint represents the average of two technical replicates from an individual experiment, with a total of n=5 independent experiments represented on the graph. One-way ANOVA with Tukey's test for multiple comparisons was utilized to assess statistical significance. **h.** The difference in percentage of double positive cells (Pulsed – Non-pulsed) from the experiment shown in **(g.)**. **i.** JY target cells were treated with 8μg/mL recombinant human perforin for 60min in perforin binding buffer, subjected to Annexin V/PI staining, and analyzed by flow cytometry. Each datapoint represents the average of two technical replicates from an individual experiment, with a total of n=3 biological experiments represented on the graph. Bars represent mean +/- SEM. Paired *t*-tests were utilized to assess statistical differences. **j.** JY cells were pre-treated with solvent or 100μM caspase-1 inhibitor VX-765 for 120mins before exposure to 8μg/mL recombinant human perforin for 60min. Cells were stained with Annexin V/PI and analyzed by flow cytometry. Data shown represents the difference between control and perforin-treated conditions for solvent-treated and VX-765-treated cells respectively. Each datapoint represents the average of two technical replicates from an individual experiment, with n=4 independent experiments shown on the graph. A paired *t*-test was utilized to assess statistical difference. *$p<0.05$, ** $p<0.01$, *** $p<0.001$, , **** $p<0.0001$, ns = not significant.

1602 **Figure 5| Melanoma cells display a pyroptotic phenotype upon CTL attack**

1603 **a-d.** Melanoma cells (D10, RIPA, and TouM3) were pulsed or non-pulsed with 10μM antigenic peptide and
1604 conjugated at an E:T ratio of 4:1 with antigen-specific human CTLs for 4hr, with JY cells as a control.
1605 Following conjugation, cells were subjected to Annexin V/PI staining and analyzed by flow cytometry. **a.**
1606 Representative dotplots of target cells from n=5 independent experiments. **b-d.** Data shown represent the
1607 percentage of cells in each quadrant of interest (Annexin V/PI double positive, Annexin V single-positive,
1608 PI single-positive) after 4hr conjugation. Each datapoint represents the average of two technical replicates
1609 from an individual experiment, with a total of n=5 independent experiments represented on the graph. Black
1610 bars represent the mean of independent experiments. One-way ANOVA with Sidak's test for multiple
1611 comparisons was utilized to assess statistical significance. **e.** D10 target cells were pulsed with 10μM
1612 antigenic peptide and conjugated with CTLs at an E:T ratio of 4:1 for 5 or 15min, before being stained with
1613 an activity-dependent caspase-1 probe and assessed using flow cytometry. Non-pulsed target cells were
1614 conjugated with CTLs under identical conditions for 15min as a control. Each datapoint represents the
1615 average of two technical replicates from an individual experiment, with n=7 independent experiments
1616 represented on the graph. One-way ANOVA with Tukey's test for multiple comparisons was utilized to
1617 assess statistical significance. **f.** D10 cells were conjugated with CTLs as above and double-stained with
1618 activity-dependent caspase-1 and caspase-3 probes before being assessed by cytometry. Cells were
1619 classified as single-positive, double-positive, or double-negative for each active caspase at each timepoint
1620 shown. Bars represent mean +/- SEM, with n=7 independent experiments. RM two-way ANOVA with
1621 Tukey's test for multiple comparisons was utilized to assess statistical significance. **g.** D10 cells were pre-
1622 treated with solvent control or the calcium chelator BAPTA-AM to inhibit calcium-dependent membrane
1623 repair mechanisms, conjugated with antigen-specific CTLs for 15min, and subjected to caspase-1 activity
1624 assay. Data represent fold increase in caspase-1 MFI, normalized to respective non-pulsed controls. Each
1625 datapoint represents the average of two technical replicates from an individual experiment, with n=8
1626 independent experiments represented on the graphs respectively. Paired *t*-tests were utilized to assess
1627 statistical significance. *$p<0.05$, ** $p<0.01$, *** $p<0.001$, **** $p<0.0001$, ns = not significant.

1628

1629 **Figure 6| Pulsed cells conjugated overnight with antigen-specific CTLs reveal a delayed apoptotic**
1630 **phenotype**

1631 **a-d.** JY and melanoma cells (D10, RIPA, and TouM3) were pulsed or non-pulsed with 10μM antigenic
1632 peptide and conjugated at an E:T ratio of 4:1 with antigen-specific human CTLs for 16hr. Following
1633 conjugation, cells were subjected to Annexin V/PI staining and analyzed by flow cytometry. Data shown
1634 represent the percentage of cells in each quadrant of interest (Annexin V/PI double positive, PI single-
1635 positive, Annexin V single-positive,) at the indicated time points. Each datapoint represents the average of
1636 two technical replicates from an individual biological experiment, with a total of n=5 independent
1637 experiments represented on the graph. One-way ANOVA with Sidak's test for multiple comparisons was
1638 utilized to assess statistical significance. *$p<0.05$, ** $p<0.01$, *** $p<0.001$, **** $p<0.0001$, ns = non-
1639 significant. NP = non-pulsed.

1640

1641 **Figure 7| Exogenous SMAPs induce target cell apoptotic cell death**

1642 **a-d.** JY cells were incubated with or without SMAPs at a protein concentration of 250 µg/mL for
1643 4 hours. Cells were subjected to Annexin V/PI staining and analyzed by flow cytometry. Data
1644 indicate the percentage of cells in each quadrant: Annexin V/PI double positive, Annexin V single-
1645 positive and PI single-positive. Each datapoint represents the average of two technical replicates
1646 from an individual biological experiment with a total of n=3 independent experiments. Statistical
1647 differences between both conditions were assessed by unpaired *t*-test for b. and c. and by Mann-
1648 Whitney test for d. ** $p < 0{,}01$, *$p < 0{,}05$, ns = not significant.

1649

1650 # List of Supplementary Movies

Supplementary Movie 1	***Target cell death upon CTL attack resembles pyroptosis and is characterized by rapid erratic membrane bubbling, formation of pyroptotic bodies, loss of membrane integrity*** JY target cells were pulsed with 10µM antigenic peptide, and conjugated at an E:T ratio of 1:1 with antigen-specific human CTLs pre-loaded with Fluo-8-AM (*green*) and SPY650 Tubulin (*magenta*) in the presence of 6.6µg/mL propidium iodide (*red*). Conjugate formation and cell death morphology was assessed using spinning disk time lapse microscopy.
Supplementary Movie 2	***Target cell death upon CTL attack resembles pyroptosis and is characterized by rapid erratic membrane bubbling, formation of pyroptotic bodies, loss of membrane integrity*** JY target cells were pulsed with 10µM antigenic peptide, and conjugated at an E:T ratio of 1:1 with antigen-specific human CTLs pre-loaded with Fluo-8-AM (*green*) and SPY650 Tubulin (*magenta*) in the presence of 6.6µg/mL propidium iodide (*red*). Conjugate formation and cell death morphology was assessed using spinning disk time lapse microscopy.
Supplementary Movie 3	***Example of pyroptotic cell death in nigericin-treated cell, characterized by erratic plasma membrane bubbling, cell swelling, and membrane rupture*** JY cells were treated with nigericin (100µM), in the presence of 6.6µg/mL propidium iodide (*red*) and imaged using spinning disk confocal microscopy.
Supplementary Movie 4	***Example of pyroptotic cell death in nigericin-treated cell, characterized by erratic plasma membrane bubbling, cell swelling, and membrane rupture*** JY cells were treated with nigericin (100µM), in the presence of 6.6µg/mL propidium iodide (*red*) and imaged using spinning disk confocal microscopy.
Supplementary Movie 5	***Example of pyroptotic cell death in nigericin-treated cell, characterized by erratic plasma membrane bubbling, cell swelling, and membrane rupture*** JY cells were treated with nigericin (100µM), in the presence of 6.6µg/mL propidium iodide (*red*) and imaged using spinning disk confocal microscopy.
Supplementary Movie 6	***Example of apoptotic cell death in staurosporine-treated cell*** JY cells were treated with staurosporine (6.7µM) in the presence of 6.6µg/mL propidium iodide (*red*) and imaged using spinning disk confocal microscopy.

Supplementary Movie 7	***Example of apoptotic cell death in staurosporine-treated cell followed by secondary necrosis*** JY cells were treated with staurosporine (6.7µM) in the presence of 6.6µg/mL propidium iodide (*red*) and imaged using spinning disk confocal microscopy.
Supplementary Movie 8	***Example of apoptotic cell death in staurosporine-treated cell*** JY cells were treated with staurosporine (6.7µM) in the presence of 6.6µg/mL propidium iodide (*red*) and imaged using spinning disk confocal microscopy.
Supplementary Movie 9	***Example of apoptotic cell death in staurosporine-treated cell*** JY cells were treated with staurosporine (6.7µM) in the presence of 6.6µg/mL propidium iodide (*red*) and imaged using spinning disk confocal microscopy.
Supplementary Movie 10	***Non-lethal interactions between non-pulsed JY cells and CTLs*** Non-pulsed JY target cells were loaded with CellMask DeepRed (*magenta*) and conjugated at an E:T ratio of 1:1 with antigen-specific human CTLs pre-loaded with Fluo-8-AM (*green*) and Tubulin Tracker Deep Red (*magenta*) for 60min and monitored by spinning disk confocal microscopy.
Supplementary Movie 11	***Target cell death upon CTL attack resembles pyroptosis and is characterized by rapid erratic membrane bubbling, formation of pyroptotic bodies, loss of membrane integrity*** JY target cells were loaded with CellMask DeepRed (*magenta*), pulsed with 10µM antigenic peptide, and conjugated at an E:T ratio of 1:1 with antigen-specific human CTLs pre-loaded with Fluo-8-AM (*green*) and Tubulin Tracker Deep Red (*magenta*) for 60min and monitored by spinning disk confocal microscopy.
Supplementary Movie 12	***Target cell death upon CTL attack resembles pyroptosis and is characterized by rapid erratic membrane bubbling, formation of pyroptotic bodies, loss of membrane integrity*** **(additional example)** JY target cells were loaded with CellMask DeepRed (*magenta*), pulsed with 10µM antigenic peptide, and conjugated at an E:T ratio of 1:1 with antigen-specific human CTLs pre-loaded with Fluo-8-AM (*green*) and Tubulin Tracker Deep Red (*magenta*) for 60min and monitored by spinning disk confocal microscopy.

1651

Figure 1

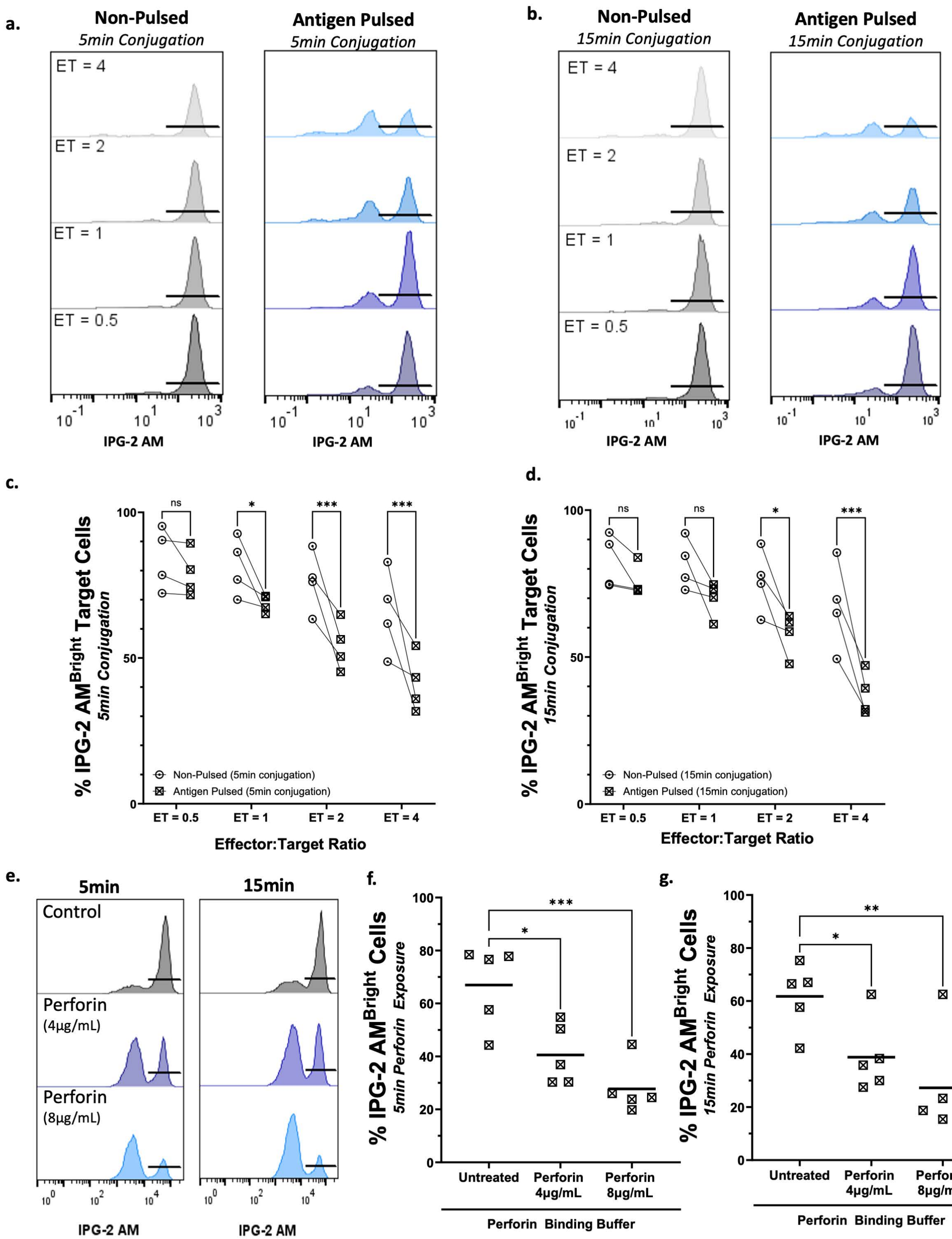
a.
Non-Pulsed
5min Conjugation
Antigen Pulsed
5min Conjugation
ET = 4
ET = 2
ET = 1
ET = 0.5
IPG-2 AM
b.
Non-Pulsed
15min Conjugation
Antigen Pulsed
15min Conjugation
c.
% IPG-2 AM Bright Target Cells
5min Conjugation
ns
*
***
***
Non-Pulsed (5min conjugation)
Antigen Pulsed (5min conjugation)
ET = 0.5
ET = 1
ET = 2
ET = 4
Effector:Target Ratio
d.
15min Conjugation
ns
ns
*
***
Non-Pulsed (15min conjugation)
Antigen Pulsed (15min conjugation)
e.
5min
15min
Control
Perforin
(4µg/mL)
Perforin
(8µg/mL)
IPG-2 AM
f.
% IPG-2 AM Bright Cells
5min Perforin Exposure
Untreated
Perforin 4µg/mL
Perforin 8µg/mL
Perforin Binding Buffer
g.
15min Perforin Exposure
**
*

Figure 2

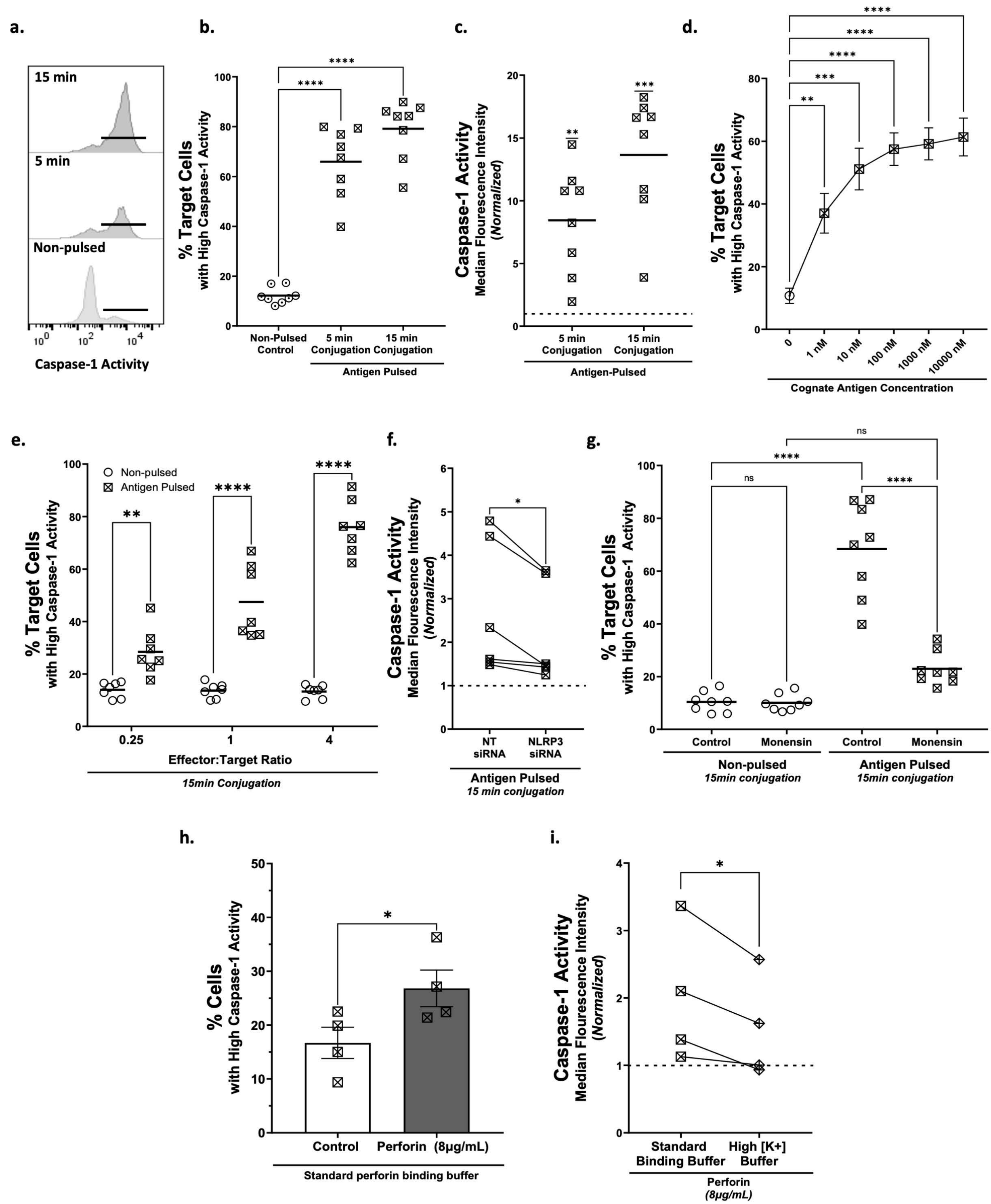
a.
15 min
5 min
Non-pulsed
Caspase-1 Activity
b.
% Target Cells
with High Caspase-1 Activity
Non-Pulsed Control
5 min Conjugation
15 min Conjugation
Antigen Pulsed
c.
Caspase-1 Activity
Median Flourescence Intensity
(Normalized)
5 min Conjugation
15 min Conjugation
Antigen-Pulsed
d.
% Target Cells
with High Caspase-1 Activity
0
1 nM
10 nM
100 nM
1000 nM
10000 nM
Cognate Antigen Concentration
e.
Non-pulsed
Antigen Pulsed
% Target Cells
with High Caspase-1 Activity
0.25
1
4
Effector:Target Ratio
15min Conjugation
f.
Caspase-1 Activity
Median Flourescence Intensity
(Normalized)
NT siRNA
NLRP3 siRNA
Antigen Pulsed
15 min conjugation
g.
% Target Cells
with High Caspase-1 Activity
ns
Control
Monensin
Control
Monensin
Non-pulsed
15min conjugation
Antigen Pulsed
15min conjugation
h.
% Cells
with High Caspase-1 Activity
Control
Perforin (8µg/mL)
Standard perforin binding buffer
i.
Caspase-1 Activity
Median Flourescence Intensity
(Normalized)
Standard Binding Buffer
High [K+] Buffer
Perforin
(8µg/mL)

Figure 3

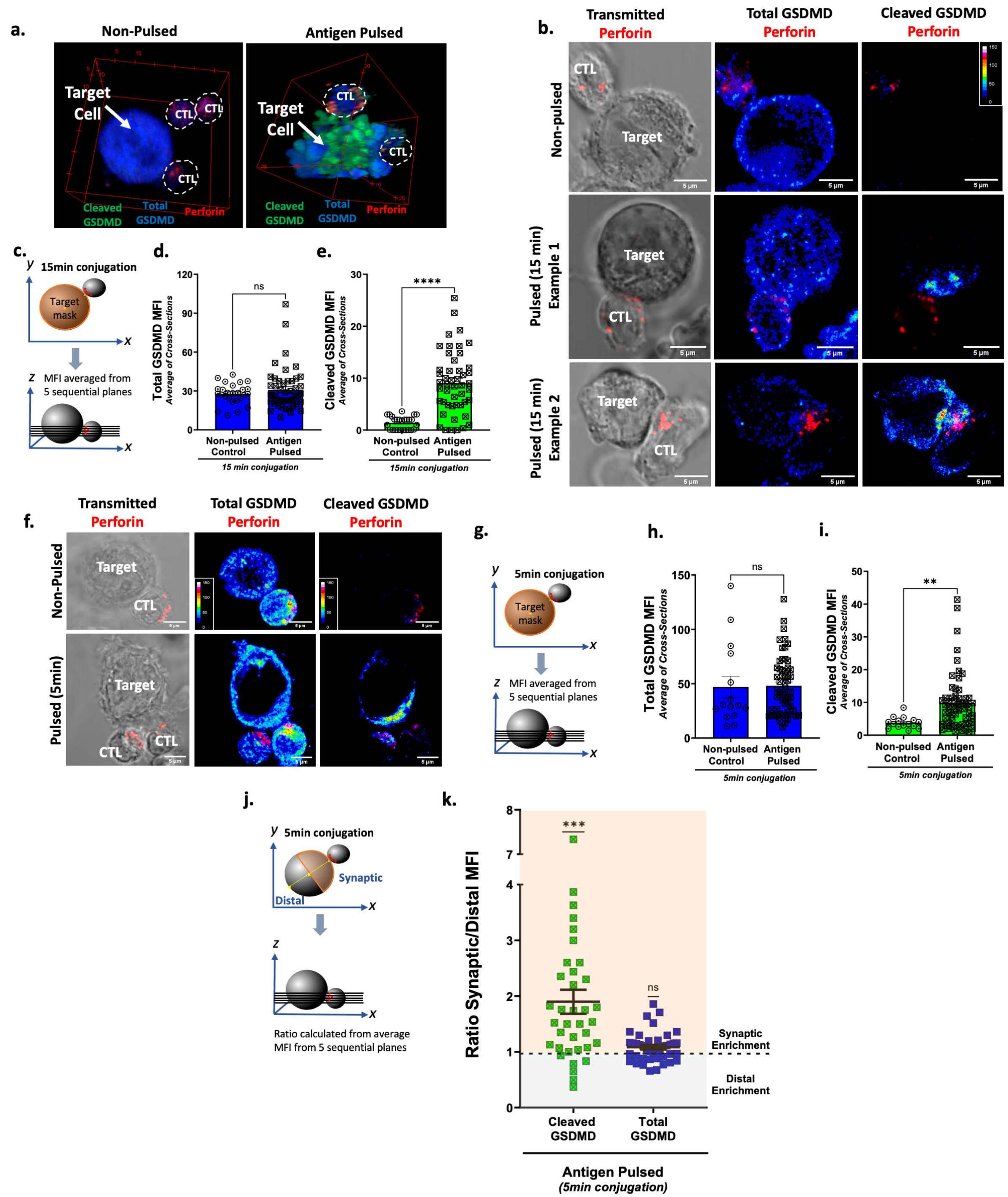
a.
Non-Pulsed
Antigen Pulsed
Target Cell
CTL
Cleaved GSDMD
Total GSDMD
Perforin
b.
Transmitted Perforin
Total GSDMD Perforin
Cleaved GSDMD Perforin
Non-pulsed
Pulsed (15 min) Example 1
Pulsed (15 min) Example 2
Target
CTL
5 µm
c.
15min conjugation
Target mask
MFI averaged from 5 sequential planes
d.
Total GSDMD MFI
Average of Cross-Sections
ns
Non-pulsed Control
Antigen Pulsed
15 min conjugation
e.
Cleaved GSDMD MFI
Average of Cross-Sections
****
15min conjugation
f.
Transmitted Perforin
Total GSDMD Perforin
Cleaved GSDMD Perforin
Non-Pulsed
Pulsed (5min)
g.
5min conjugation
h.
Total GSDMD MFI
Average of Cross-Sections
ns
5min conjugation
i.
Cleaved GSDMD MFI
Average of Cross-Sections
**
5min conjugation
j.
5min conjugation
Synaptic
Distal
Ratio calculated from average MFI from 5 sequential planes
k.
Ratio Synaptic/Distal MFI
***
ns
Synaptic Enrichment
Distal Enrichment
Cleaved GSDMD
Total GSDMD
Antigen Pulsed
(5min conjugation)

Figure 4

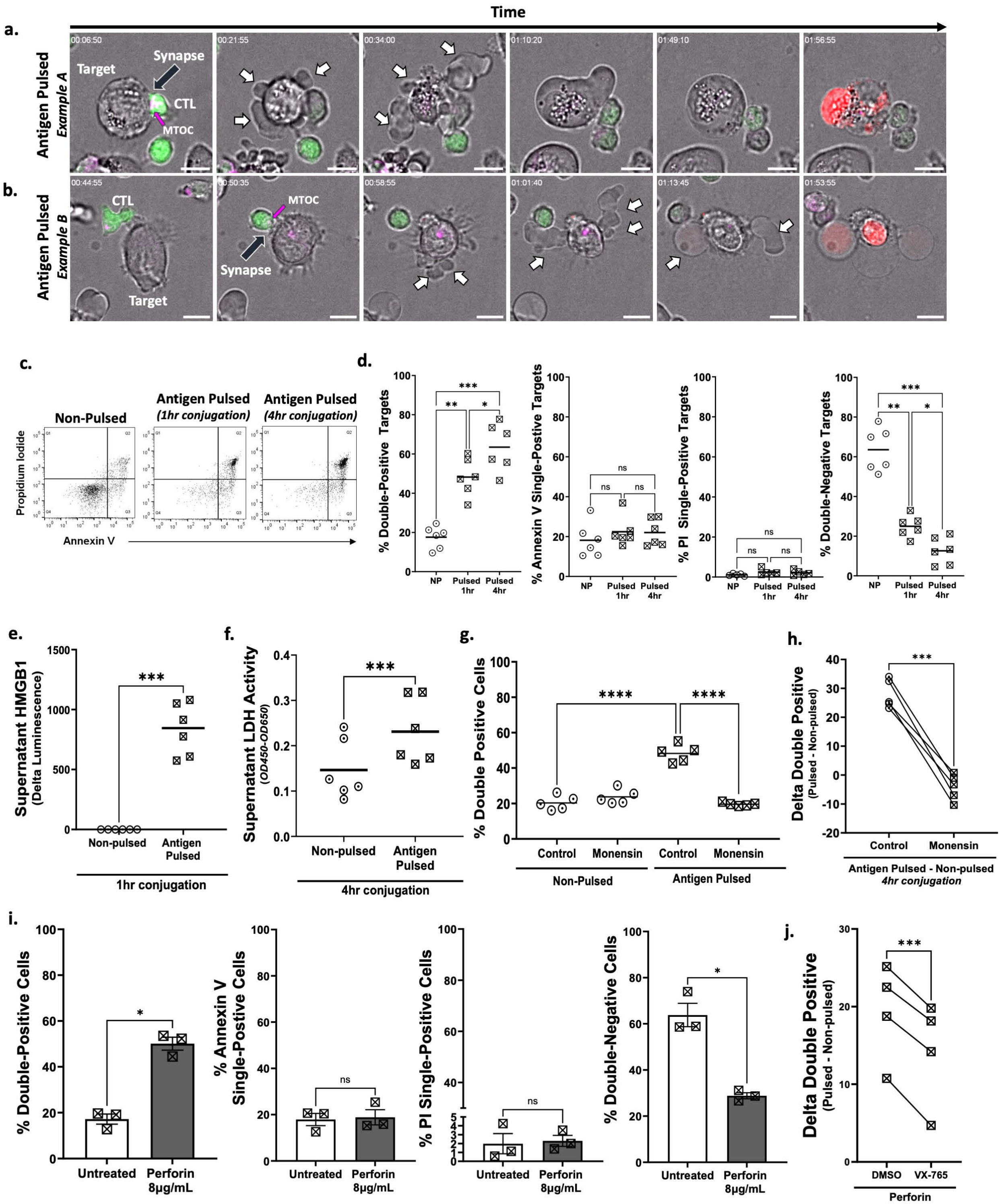
Time
a.
Antigen Pulsed
Example A
Target
Synapse
CTL
MTOC
00:06:50
00:21:55
00:34:00
01:10:20
01:49:10
01:56:55
b.
Antigen Pulsed
Example B
CTL
Target
MTOC
Synapse
00:44:55
00:50:35
00:58:55
01:01:40
01:13:45
01:53:55
c.
Non-Pulsed
Antigen Pulsed
(1hr conjugation)
Antigen Pulsed
(4hr conjugation)
Propidium Iodide
Annexin V
d.
% Double-Positive Targets
% Annexin V Single-Postive Targets
% PI Single-Positive Targets
% Double-Negative Targets
NP
Pulsed 1hr
Pulsed 4hr
ns
e.
Supernatant HMGB1
(Delta Luminescence)
Non-pulsed
Antigen Pulsed
1hr conjugation
f.
Supernatant LDH Activity
(OD450-OD650)
4hr conjugation
g.
% Double Positive Cells
Control
Monensin
Non-Pulsed
Antigen Pulsed
h.
Delta Double Positive
(Pulsed - Non-pulsed)
Antigen Pulsed - Non-pulsed
4hr conjugation
i.
% Double-Positive Cells
% Annexin V Single-Postive Cells
% PI Single-Positive Cells
% Double-Negative Cells
Untreated
Perforin 8μg/mL
j.
Delta Double Positive
(Pulsed - Non-pulsed)
DMSO
VX-765
Perforin

Figure 5

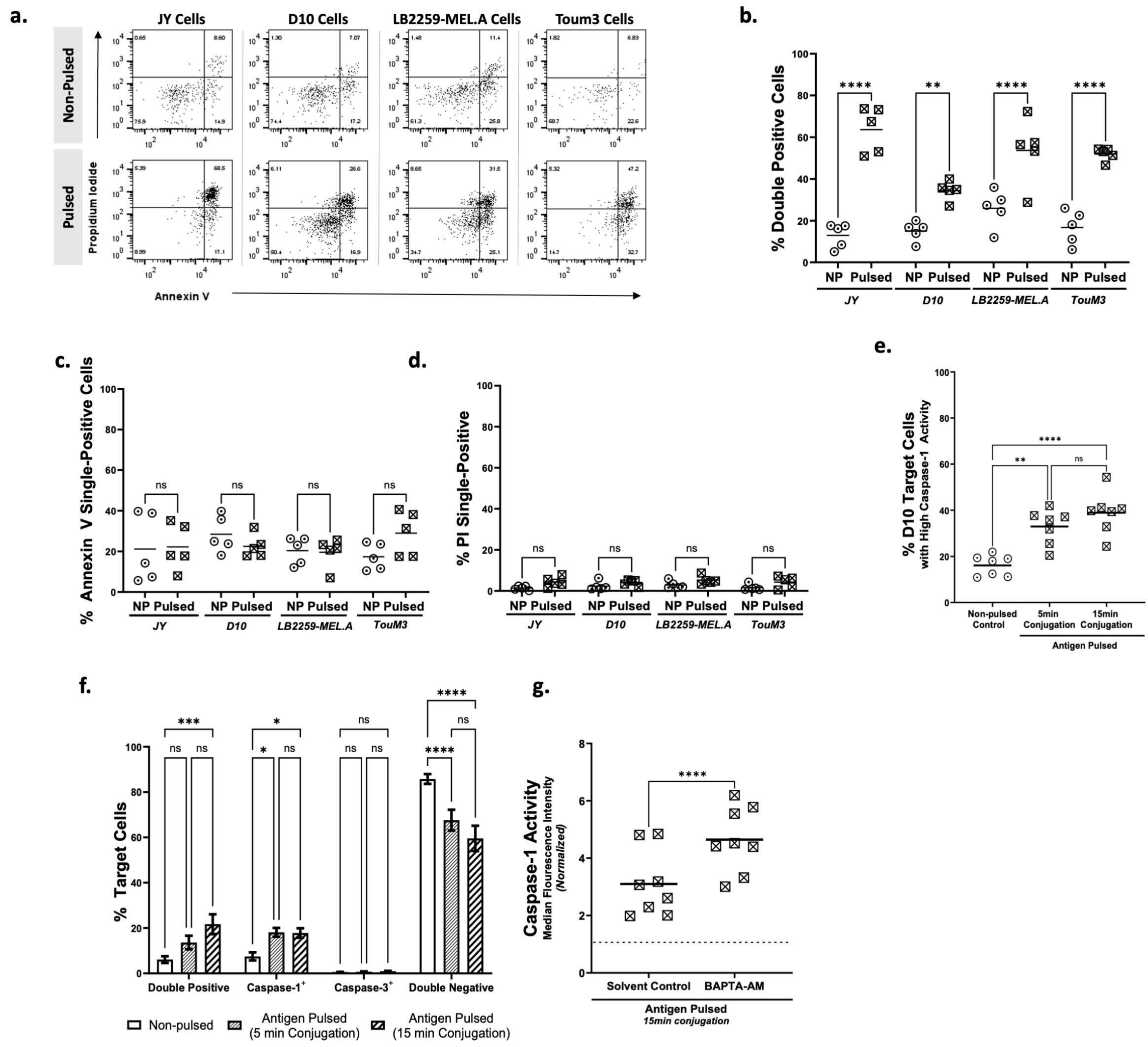
a.
JY Cells
D10 Cells
LB2259-MEL.A Cells
Toum3 Cells
Non-Pulsed
Pulsed
Propidium Iodide
Annexin V
b.
% Double Positive Cells
NP Pulsed
JY
D10
LB2259-MEL.A
TouM3
c.
% Annexin V Single-Positive Cells
ns
d.
% PI Single-Positive
e.
% D10 Target Cells with High Caspase-1 Activity
Non-pulsed Control
5min Conjugation
15min Conjugation
Antigen Pulsed
f.
% Target Cells
Double Positive
Caspase-1+
Caspase-3+
Double Negative
Non-pulsed
Antigen Pulsed (5 min Conjugation)
Antigen Pulsed (15 min Conjugation)
g.
Caspase-1 Activity
Median Flourescence Intensity (Normalized)
Solvent Control
BAPTA-AM
Antigen Pulsed
15min conjugation

Figure 6

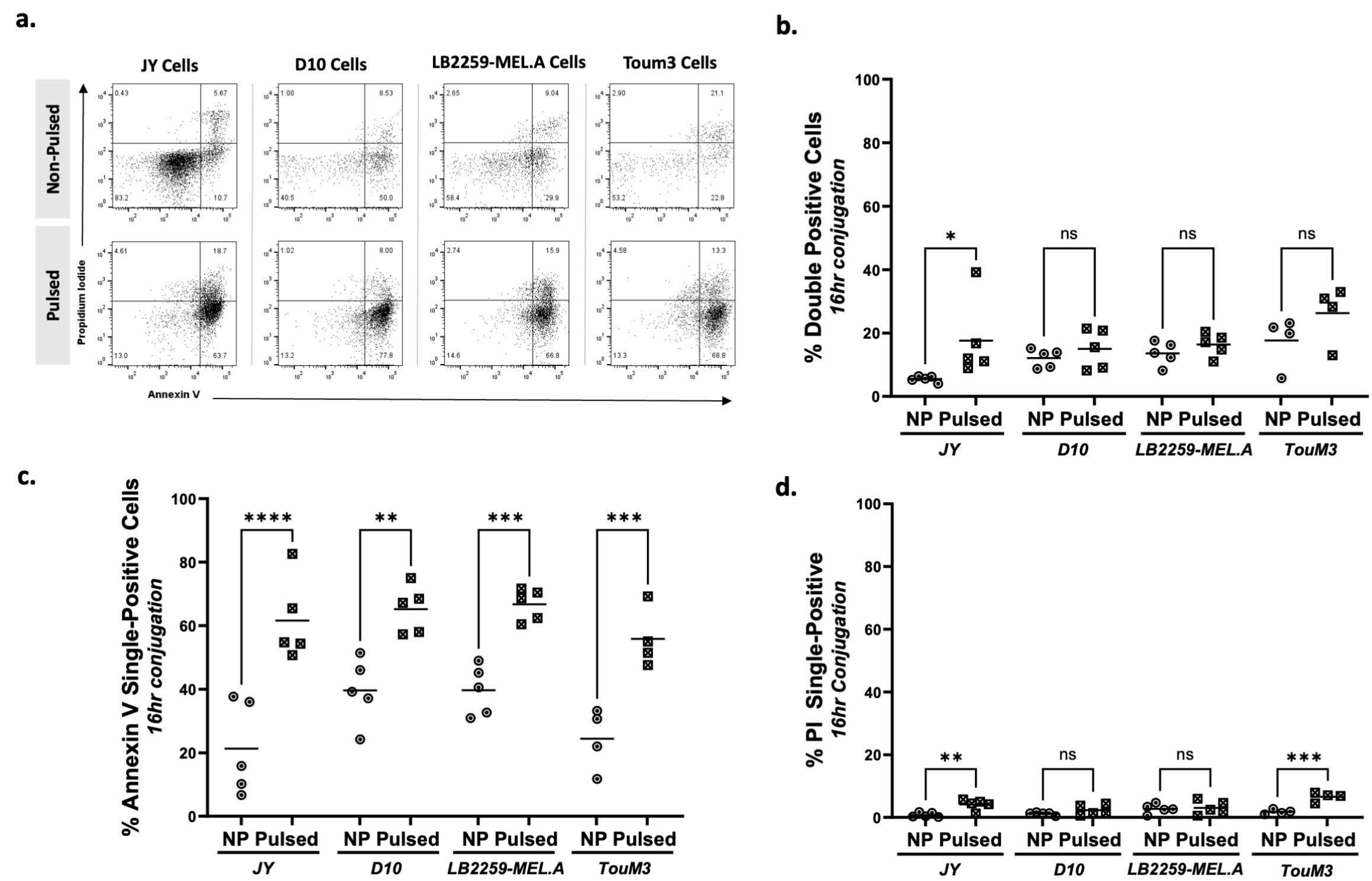
a.
JY Cells
D10 Cells
LB2259-MEL.A Cells
Toum3 Cells
Non-Pulsed
Pulsed
Propidium Iodide
Annexin V
b.
% Double Positive Cells
16hr conjugation
NP Pulsed
JY
D10
LB2259-MEL.A
TouM3
c.
% Annexin V Single-Positive Cells
16hr conjugation
d.
% PI Single-Positive
16hr Conjugation

Figure 7

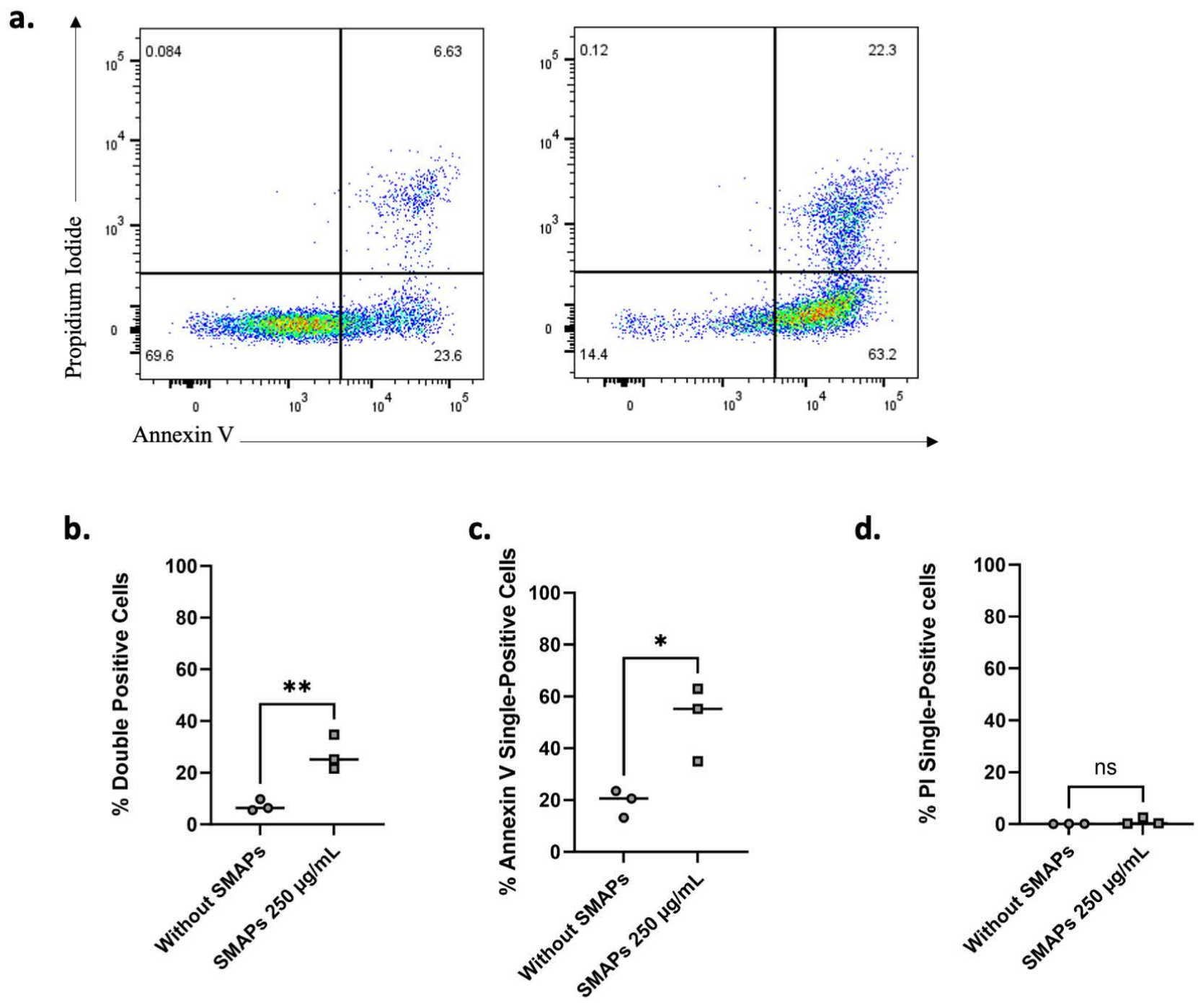
a.
Propidium Iodide
Annexin V
0.084
6.63
69.6
23.6
0.12
22.3
14.4
63.2
b.
% Double Positive Cells
**
Without SMAPs
SMAPs 250 µg/mL
c.
% Annexin V Single-Positive Cells
*
Without SMAPs
SMAPs 250 µg/mL
d.
% PI Single-Positive cells
ns
Without SMAPs
SMAPs 250 µg/mL